



Politecnico di Torino
Department of Applied Science and Technology
Master's thesis in Materials Engineering

**Electrochemical sensors functionalized with
 $\text{Bi}_5\text{O}_7\text{NO}_3/\text{Bi}_2\text{O}_3$ heterostructures for non-enzymatic
paracetamol sensing: Theoretical model and
characterization**

Candidate:
Filippo Franceschini

Supervisors:

Prof. Sandro Carrara (EPFL)

Prof. Alberto Tagliaferro (PoliTo)

Dr. Mattia Bartoli (PoliTo)

October 2021

An expert is a person who has made
all the mistakes that can be made
in a very narrow field.
— Niels Bohr

To my family and friends.

Acknowledgements

This manuscript is the result of more than six months of work divided evenly between the Polytechnic of Turin and the École Polytechnique Fédérale de Lausanne. A clear thematic division can be discerned between the research pursued during the first period in Italy and the second in Switzerland. In the same way an apparent distinction between the two experiences emerges, now that i look back at the end of the road. Both equally exceptional and truly formative. In Italy i had the great pleasure of working day to day with Dr. Mattia Bartoli, who not only listened to my mental lucubrations and dubious interpretations, but also instilled in me a great passion for doing science, just because it's fun. Equally important has been Prof. Alberto Tagliaferro, who has always graciously directed me towards asking the right questions while critiquing my own answers, especially when tackling statistics and solid state physics. Moreover, the days at the laboratory would not have been as fun without Giovanni, Andrea, Cristian and Solomya. I'm very grateful for their friendship and for always inspiring to do better. Possibly one of the greatest takeaways of the mostly theoretical study done at PoliTo has been not to be scared to explore difficult topics, and that being confused is just the first step to a deep comprehension. In Switzerland i was fortunate enough to be able to consult with Prof. Sandro Carrara, who with great patience listened to any doubts or problems that would arise. I will look back with great fondness to the coffee breaks and goodbye parties where all of us students would listen to the stories of the Prof. and share laugh. Finally in Switzerland i also had the privilege of meeting great scientists-in-training such as Riccardo and Gianluca with whom i thoroughly enjoyed to discuss, while always learning something from them.

Turin, October 2021

F. F.

Abstract

Given the risks associated with liver transplant operations and the protagonist role of paracetamol overdose in cases of hepatotoxicity, there's a growing need for a fast, cheap and easy to use method for its detection. Compared to traditional methods like HPLC, spectrophotometry, colourimetry and chemiluminescence, electrochemical sensors have the potential of reaching less fortunate hospitals that cannot afford expensive equipment and serve as a quick point-of-care screening method for suspected cases of paracetamol toxicity. Moreover in the field of therapeutic drug monitoring a lot of effort has been put in developing electrochemical sensors to better control the depth of anesthesia, where paracetamol is usually a component. Enzymatic biosensors have the disadvantage of being generally unstable and sensitive to pH and temperature variations. Non-enzymatic electrochemical sensors overcome some of these limitations showing very good sensitivities and limit of detection, though at the cost of limited specificity. In this work a computational study was initially performed, based on a semi-empirical method (PM3). The interaction of a molecule of Paracetamol with a cluster of $\text{Bi}_5\text{O}_7\text{NO}_3$ is evaluated and then through the use of Marcus theory the rate constant for electron transfer is obtained. Such an investigation allowed to set a theoretical framework for the study of defect design. In particular, through a solid state method different heterostructures of $\text{Bi}_2\text{O}_3/\text{Bi}_5\text{O}_7\text{NO}_3$ were produced with the objective of exploring their role as potential electrocatalysts. Their performance was evaluated by cyclic voltammetry on commercial screen printed electrodes by Dropsens[®], where the working electrode was functionalized with an aqueous dispersion of the produced catalysts. Through the use of Laviron equation a kinetic study was performed and the rate constants of electron transfer calculated. A good agreement was found between the values of rate constant obtained through experimental and computational means. Furthermore, the electrocatalytic activity of the heterostructures was identified as superior to that of single phase subnitrate. This was both observed both in the kinetic study and in the calibration curves. From a morphological study done with the Scanning Electron Microscope (SEM), it was also remarked that the partial oxidation of the bismuth subnitrate induces a change in shape, from particular to lamellar. Based on the electrochemical tests performed, and the knowledge acquired in the theoretical work, the best performing material is selected for the fabrication of a paper-based biosensor.

List of Acronyms

LOD Limit of Detection	51
SPE Screen Printed Electrodes	ix
PCM Paracetamol	viii
TST Transition State Theory	9
ET Electron Transfer	9
PES Potential Energy Surface	9
TSA Two State Approximation	10
EC electrochemical	2
WE Working Electrode	18
CE Counter Electrode	18
NAPQI N-acetyl-p-benzoquinoneimine	5
RE Reference Electrode	18
SHE Standard Hydrogen Electrode	18
NHE Normal Hydrogen Electrode	18
CV Cyclic Voltammetry	23
Ox oxidized species	23
Red reduced species	24
SCF Self Consistent Field	15

HF Hartree-Fock	16
TDM Therapeutic Drug Monitoring	4
PBS Phosphate Buffer Saline	viii
DI Deionized	x
EIS Electrochemical Impedance Spectroscopy	43
XPS X-ray Photoelectron Spectroscopy	45
XRD X-ray Diffraction Analysis	45
SD Standard Deviation	51
RSD Relative Standard Deviation	51
SEM Scanning Electron Microscope	iii
HOMO Highest Occupied Molecular Orbital	x
LUMO Lowest Unoccupied Molecular Orbital	x

Contents

Acknowledgements	i
Abstract	iii
List of Acronyms	v
List of figures	ix
List of tables	xiii
1 Introduction	1
1.1 Biosensors	1
1.2 Paracetamol sensing	5
1.3 Nanomaterials as electrocatalysts for non enzymatic sensors	6
1.4 Bismuth and bismuth related compounds	7
1.5 The aim of this research	8
2 Theoretical Background	9
2.1 Electron transfer theories	9
2.1.1 Libby Theory	11
2.1.2 Classical Marcus Theory	12
2.1.3 Generalized Marcus Theory	14
2.1.4 Generalized Mulliken Hush Theory	15
2.2 Semiempirical computational methods	15
2.3 Theoretical principles of electrochemical sensors	18
2.3.1 Mass transfer and Fick's laws of diffusion	19
2.3.2 Reversibility and Nernst equation	20
2.3.3 Electrochemical kinetics and Butler-Volmer equation	21
2.3.4 Cyclic Voltammetry	23
3 Materials and Methods	27
3.1 Computational study	27
3.1.1 Bismuth cluster	27
3.1.2 Paracetamol	28
3.2 Materials synthesis	29

3.3	Screen printed electrode functionalization	29
3.4	Cyclic voltammetry analysis parameters	31
3.5	Phosphate Buffer Saline (PBS) and Paracetamol (PCM) solutions preparation	31
3.6	Carbon paper-based electrochemical cell for preliminary test	32
3.6.1	Carbon paper functionalization	32
3.6.2	Carbon paper-based working electrode fabrication	32
3.6.3	Electrochemical cell assembly	33
3.7	Paper-supported electrochemical sensor fabrication	33
4	Results and Discussion	35
4.1	Computational model	35
4.1.1	Calculated rate constant and activation energy	40
4.2	Cyclic Voltammetry	41
4.2.1	Electrochemical oxidation of Paracetamol in aqueous solutions	41
4.2.2	Preliminary electrochemical evaluations of the system	42
4.2.3	Detailed characterization and kinetic study	44
4.2.4	Limit of detection and calibration curves	50
4.3	Morphological characterization	53
4.4	Raman Spectra	55
5	Appendix	59
5.1	Preliminary test on a C-paper modified electrochemical cell	59
5.2	Paper based electrode proof-of-concept results	61
6	Conclusions	63
	Bibliography	73

List of Figures

1.1	Macro-fields of application of electrochemical biosensors	2
1.2	Typical example of a Screen Printed Electrodes (SPE) and its constituent components	4
1.3	Main causes of acute liver failure and the comparative effect of PCM overdose in the U.S as reported by <i>Stravitz et al</i> [25]	5
1.4	Bismuth oxide phases and evolution of bismuth nitrate salt. Reproduced with permission from Bartoli <i>et al.</i> [48]	8
2.1	Potential Energy Surface	9
2.2	Adiabatic and Non-adiabatic processes	11
2.3	Reactants and products with solvent	12
2.4	Formation of the collision complex and subsequent electron transfer	13
2.5	Two types of three electrode systems	18
2.6	Current-overpotential relationship according to BV theory	22
2.7	Cyclic voltammogram and excitation signal	23
3.1	Cluster of $\text{Bi}_5\text{O}_7\text{NO}_3$	28
3.2	Optimized molecule of Paracetamol	28
3.3	Example of a sample obtained after calcination	29
3.4	Drop casting setup with the help of an optical microscope	30
3.5	Preparation procedure for the different concentrations of PCM + PBS	31
3.6	Flowchart of the deposition process	32
3.7	Carbon paper-based working electrode under optical microscope for the measurement of its area	33
3.8	Electrochemical cell setup	33
3.9	Paper-supported electrochemical sensor	34
4.1	Paracetamol and $\text{Bi}_5\text{O}_7\text{NO}_3$ cluster optimized geometry	36
4.2	Examples of alternative optimizations for different interactions geometries	37
4.3	Charge density for a plane passing through the aromatic ring of PCM and through the interacting Bi atoms of the cluster	38
4.4	Charge density for a plane passing through the aromatic ring of paracetamol and perpendicular to the axis of the two Bi atoms of the cluster interacting with PCM	38

4.5	Highest Occupied Molecular Orbital (HOMO) of the system PCM- Bi ₅ O ₇ NO ₃ cluster	39
4.6	Lowest Unoccupied Molecular Orbital (LUMO) of the system PCM- Bi ₅ O ₇ NO ₃ cluster	39
4.7	Cyclic voltammogram of 1mM of paracetamol in 0.1M of PBS at pH 7.4 on a SPE	41
4.8	Cathodic and anodic current peak ratio as a function of pH for paracetamol, as reported by Nematollahi <i>et al.</i> [29]	42
4.9	(a) With and without PCM for a bare electrode, (b) Adsorption of PCM on a bare electrode after cleaning with Deionized (DI) water three times	43
4.10	(a) Current peak ratio as a function of scan rate for a bare electrode at a PCM concentration of 1mM, (b) Current peak ratio as a function of PCM concentration for a bare electrode	43
4.11	Comprehensive overview of the voltammograms for the differently functionalized SPEs at a scan rate of 100mV/s in PBS at pH 7.4 and PCM concentration of 1mM	44
4.12	(a) Cyclic voltammograms at different scan rates (from 50mV/s to 300mV/s in steps of 50mV/s) for a solution of 0.1M PBS with 1mM of PCM for a bare SPE, with the linear dependence of the peak currents on the square root of the scan rate, (b) plots showing the linear relationship of ΔE_p and E_{pa} , E_{pc} from $\ln(v)$.	46
4.13	(a) Cyclic voltammograms at different scan rates (from 50mV/s to 300mV/s in steps of 50mV/s) for a solution of 0.1M PBS with 1mM of PCM for a B500 functionalized SPE, with the linear dependence of the peak currents on the square root of the scan rate, (b) plots showing the linear relationship of ΔE_p and E_{pa} , E_{pc} from $\ln(v)$	48
4.14	(a) Cyclic voltammograms at different scan rates (from 50mV/s to 300mV/s in steps of 50mV/s) for a solution of 0.1M PBS with 1mM of PCM for a B450 functionalized SPE, with the linear dependence of the peak currents on the square root of the scan rate, (b) plots showing the linear relationship of ΔE_p and E_{pa} , E_{pc} from $\ln(v)$	48
4.15	(a) Cyclic voltammograms at different scan rates (from 50mV/s to 300mV/s in steps of 50mV/s) for a solution of 0.1M PBS with 1mM of PCM for a B600 functionalized SPE, with the linear dependence of the peak currents on the square root of the scan rate, (b) plots showing the linear relationship of ΔE_p and E_{pa} , E_{pc} from $\ln(v)$	49
4.16	(a) Cyclic voltammograms at different scan rates (from 50mV/s to 300mV/s in steps of 50mV/s) for a solution of 0.1M PBS with 1mM of PCM for a B525 functionalized SPE, with the linear dependence of the peak currents on the square root of the scan rate, (b) plots showing the linear relationship of ΔE_p and E_{pa} , E_{pc} from $\ln(v)$	49
4.17	Overview of the calibration curves for the differently functionalized SPEs at a scan rate of 100mV/s in PBS at pH 7.4 and PCM concentration of 0.5mM, 1mM, 2mM, 3mM	50

4.18	Calibration curves for the different SPE studied, obtained at scan rate of 100mV/s and concentrations of PCM of 0.5mM, 1mM, 2mM,3mM in 0.1M PBS	52
4.21	Raman analysis of different materials obtained by solid state synthesis	55
4.22	Vibrational moment associated with the Raman peak at 1049 cm^{-1}	56
4.23	Fitting of NO_3^- peak for B400	56
4.24	Fitting of small peaks for B525	57
4.25	Fitting of Bi_2O_3 peaks	57
5.1	Comprehensive overview of the voltammograms for the differently functionalized carbon paper electrodes at a scan rate of 100mV/s in PBS at pH 7.4 and PCM concentration of 1mM	59
5.2	(a) First iteration of a paper based electrode at a scan rate of 50mV/s in PBS at pH 7.4 and PCM concentration of 3mM (b) Second iteration of a paper based electrode at a scan rate of 150mV/s in PBS at pH 7.4 and PCM concentration of 3mM	61

List of Tables

2.1	Useful properties of reversible processes	25
3.1	Calcination temperatures of the different samples	29
3.2	Setting parameters for the Cyclic Voltammetry analysis	31
4.1	Fictitious bond lengths of the different computed configurations	36
4.2	Rate constant and activation energy of the optimized structure	40
4.3	Anodic peak currents for the different functionalized materials	44
4.4	Energetic and kinetic parameters for the different materials, where k and D are calculated at a scan rate of 100 mV/s	45
4.5	Fitting parameter for anodic and cathodic peak currents with respective coeffi- cient of determination	47
4.6	Linear regression equation for ΔE_p with respect to the logarithm of the scan rate	47
4.7	Sensitivity and limit of detection for the different modified electrodes	50
4.8	Fitting parameters for the calibration curves	51
5.1	Anodic peak currents for the different functionalized materials	60
5.2	Summary of relevant parameters of a tentative study of carbon paper electrodes functionalized with the synthesized materials	60
5.3	Carbon paper electrodes dimension variability expressed in terms of relative standard deviation	60

1 Introduction

The aim of this introductory chapter is to provide a brief review of the state of the art of electrochemical sensors. The bioelement-free sensors produced in this work and the widely diffused biosensors show strong overlap, not only in terms of fabrication techniques but also in the applications where they are employed. For this reason a general overview of biosensors will be presented. An implicit decision is made to refer to a broad understanding of the term biosensor itself, whilst acknowledging the definition proposed by IUPAC. Moreover, to provide a better understanding on the motivation and the need for paracetamol sensing a summary of the main justifications is carried out. In particular the metabolic pathways leading to hepatotoxicity and the neurotoxic effect on aquatic fauna is discussed. At the same time the main points regarding the use of nanomaterials as electrocatalysts are examined, with a short mention to the field of defect engineering. Lastly, the element bismuth and its compounds are explored, with particular attention to their use as efficient, cheap and relatively "green" catalysts.

1.1 Biosensors

The term "biosensor" was first introduced by Cammann in 1977 [1], and even though a multitude of definitions have been proposed, the one advanced by Higson [2] is probably the most concise:

" [...] a chemical sensing device in which a biologically derived recognition entity is coupled to a transducer, to allow the quantitative development of some complex biochemical parameter."

Accordingly, two main components have been historically identified in a biosensor: a transducer and a bioelement. When a measurement is performed the analyte molecule interacts in a specific way with the bioelement (such as an enzyme or an antibody) which is coupled to a transducer that translates the response of the bioelement in an electrical signal. Even though such a definition is also supported by IUPAC, nowadays for practical reasons in the literature

it's common to refer to sensors free of biorecognition elements as biosensors when they serve the same purpose of common biosensors. It's possible to distinguish different kinds of biosensors based on the nature of the transducer employed: optical, mass based, calorimetric and electrochemical [3], [4]. Notably, electrochemical (EC) biosensors are particularly significant, not only for the vast applications they have but also from an historical point of view. In fact, the first biosensor to be fabricated was based on the enzyme glucose oxidase and developed in 1962 by the scientist Leland C. Clark.



Figure 1.1 – Macro-fields of application of electrochemical biosensors

In general EC biosensors can be further distinguished in potentiometric, amperometric, conductometric or impedimetric sensors, on the basis of the physical parameter being measured. Potentiometric sensors measure the change in potential produced by the interaction with the analyte of interest with the transducer, whereas conductometric sensors evaluate the perturbation in conductivity produced in an electrochemical cell composed of two electrodes separated by a solution. Instead, one refers to impedimetric sensors if they are based on the measurement of the cell complex impedance through the application of excitation signal variable in frequency (usually $0.01-10^5$ Hz). So as a consequence of the target molecule adsorbing on the electrode surface, or interacting specifically with a bioelement, a change in impedance can be discerned. Finally, amperometric sensors measure the flow of current induced by the oxidation or reduction reaction of an electroactive species: this is the kind of sensors on which this study focuses on.

EC biosensors have proved to be promising alternatives to conventional analytical instruments in a multitude of applications, paving the way for truly portable, in situ devices given their potential to be miniaturized. A brief summary is presented in **Figure 1.1**, where the main macro-fields of application are described. In the context of food safety analysis traditional approaches like mass spectroscopy, gas chromatography or high performance liquid chromatography are usually done at the final stage of a production process, are expensive and require trained operators to use them. Whereas EC biosensors have shown to be a powerful alternative, allowing fast, cheap and onsite measurement of relevant analytes such as antibiotics, toxins and allergens [5]. Consequently their implementation could translate in potential

indirect savings avoiding for instance that contaminated batches go through unnecessary steps before being eventually discarded.

Recently the detection of pollutants through electrochemical means has also been fruitful, granting a fast and simple identification of petroleum pollutants [6], persistent pesticides such as organophosphorus compounds, or organic pollutants like polycyclic aromatic hydrocarbons (PAH) [7]. As with most cases the use of a biosensor drastically reduces the cost and expertise required to make a measurement. This is true also for the detection of air pollutants, which is traditionally done through an expensive system composed of a sampling device coupled to a gas chromatographer/mass spectrometer.

Moreover the use of biosensors for clinical diagnosis has also seen significant interest in the recent years [8], accompanied by a shift in clinical practice from treatment to prevention and early diagnosis. Numerous analytes are currently under study, but particular attention has been put towards the detection of glucose, cholesterol, DNA, ATP, antigens and antibodies [9]. A few obstacles still need to be overcome for a widespread commercial distribution of EC biosensors for diagnostic purposes. Particularly critical factors to control are their stability, reproducibility and the interference of other species which are electrochemically active in the same potential range [9]. A notable case of successful implementation in clinical practice of an EC biosensor is in the measurement of glucose, revolutionizing the management of diabetic disease. In fact, through the use of a portable glucose-sensing device the patient is empowered to take better control over their health, meaning more frequent testing and improvement of his outcomes [10]. As of now, most glucose sensors are based on the immobilization of the enzyme glucose oxidase on the surface of the sensor. Although cheap and easy to produce, their main limitation is the intrinsic instability of the enzyme, rendering the sterilization process during manufacturing complex and requiring care not to exceed temperature and humidity safety levels during stocking [11]. For these reasons in the last 10 years a lot of work has been put in trying to develop non enzymatic sensors for diabetic patients which exploit the electrocatalytic oxidation of glucose. Many solutions have been proposed, and most are based on nanostructured materials, which are known to be very effective catalysts, thanks to the high proportion of uncoordinated atoms due to their high specific surface area [12]. Despite the many advantages compared with enzymatic sensing, their inferior specificity and higher manufacturing cost limits their use, for now.

Possibly one of the most important contributions in the push towards miniaturized electrochemical sensors has been the implementation of screen printing techniques. Simply put these manufacturing methods require the use of a screen, usually of polymeric material, and multiple layers of ink which are selectively deposited on the exposed area of the biosensor's support through the use of a squeegee. In a typical process, a Ag/AgCl based ink will be used for the electrical contacts and for the reference electrode, then for the counter and working electrode a carbon-based ink will be employed. Then if needed a functionalization of the working electrode surface will be done, be it through the use of an enzyme or a catalyst. The most frequent techniques for the enzyme immobilization on the working electrode are physical entrapment, non-covalent adsorption, bio-conjugation or covalent adsorption [13]. Different techniques can be employed for the modification of the working electrode through

the deposition of metal or metal oxide nanoparticles. The most commonly employed methods are drop casting, ink mixing or electrodeposition [14]. At the end of the process a protective layer, made out of wax for instance, will be printed to clearly define the area of interaction with the analyte and to protect the electrical contacts.

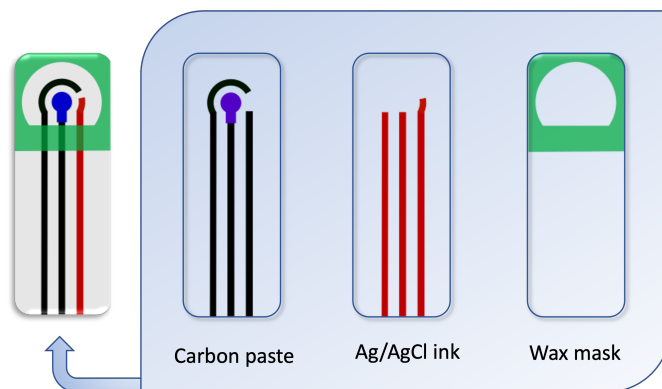


Figure 1.2 – Typical example of a SPE and its constituent components

The reason for the broad diffusion of screen printed biosensors can be attributed to their fast response, high sensitivity, ease of fabrication, linear output and ability to operate at room temperature [15]. Importantly they can be mass produced and still show a relatively consistent electrochemical response. One of the most exciting consequences of the diffuse fabrication of SPE is the development of wearable EC devices for sweat [16], saliva [17] or tear sensing [18]. These devices can be designed for instance to obtain accurate and real time indication of the concentration of ions (Na^+ , Cl^- , Li^+), having important implications for the treatment of schizophrenia or simply for continuous feedback regarding potential dehydration during exertion.

The research in last 50 years has pointed out that drug concentration in bodily fluids (usually plasma or blood) is a good indication of the pharmacological activity of drugs [19]. A correct determination of the ideal dosage is critical for drugs that have a low tolerability and pose a risk for toxicity. A novel solution to the problem of dosage determination is offered by the approach known as Therapeutic Drug Monitoring (TDM). Briefly, it consist in acquiring an accurate measurement of the drug concentration and to adjust the dosage accordingly so as maintain it always in the therapeutic range. Current techniques are based on immunoassays, spectrometric analysis or separation sciences [20]. The main disadvantage of separation-based techniques is the fact that are labour intensive and time consuming. Immunoassays similarly are complicated by the multiple steps required to run the analysis. Even though the ELISA technique allows multiplexing, it usually requires a minimum amount of samples to be cost efficient. EC biosensors in general do not suffer these limitations¹, and have the great advantage of offering a real time measurement and requiring a low sample volume. This last aspect is particularly significant because TDM is commonly performed on bodily fluids, thus

¹It should be noted that also optical biosensors are being developed, but it's beyond the scope of the brief review

to minimize the required volumes means to minimize the patient's discomfort. As an example, in the field of oncology and interesting development is represented by the work of Alvau *et al.* [21] for the detection of Irinotecan, an anticancer drug, where the bioelement immobilized on the transducer is an enzyme. In the context of personalized therapy Stradolini *et al.* [22] have developed a non enzymatic EC biosensor with the aim of better controlling the depth of anesthesia. In this particular system through the use of a feedback loop a balanced delivery of appropriate drugs is delivered, of which paracetamol is a component.

1.2 Paracetamol sensing

PCM (also referred to as Acetaminophen) is one of the most commonly used drugs in the world, being used as an antipyretic, analgesic, non steroidal anti-inflammatory drug (NSAID) [23]. The mechanism of action is still under study, but it appears to inhibit the cyclooxygenase activity in the brain and the synthesis of prostaglandins [24]. Under the correct therapeutic dosage, no side effects are reported. However, in case of overdose liver and kidney damage are a frequent consequence. In fact, PCM toxicity is the leading cause of acute liver failure in the U.S. (shown in **Figure 1.3**) [25] which leads to liver transplant for approximately 30% of the cases. The metabolism of PCM under therapeutic dosages takes place in the liver mostly

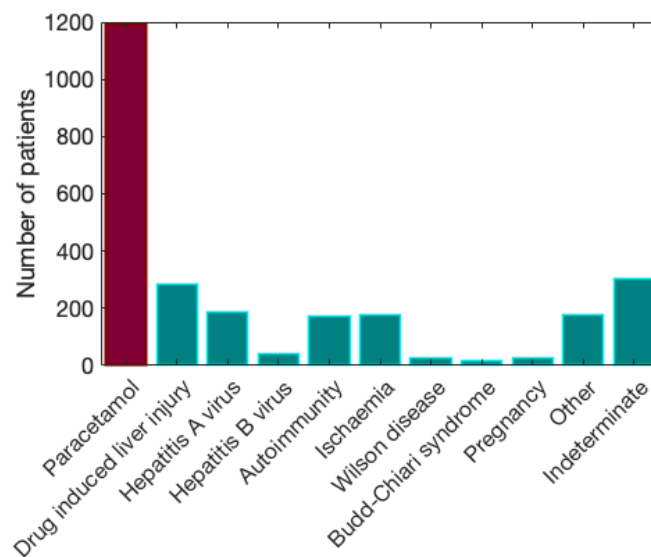


Figure 1.3 – Main causes of acute liver failure and the comparative effect of PCM overdose in the U.S as reported by *Stravitz et al* [25]

through glucuronidation and sulfuration pathways. However these tend to get saturated for higher dosages, allowing the cytochrome P450 to metabolize significant quantities of PCM to the electrophilic N-acetyl-p-benzoquinoneimine (NAPQI), which in turn gets reduced by glutathione in non toxic compounds [26]. At a certain point the reserves of glutathione become depleted and the concentration of NAPQI increases in the liver. Accordingly by

progressively binding to hepatic macrophagic cells NAPQI causes irreversible cell death, thus hepatic necrosis. Other non-P450 metabolic mechanisms leading to NAPQI and activated by myeloperoxidases and cyclooxygenase [27] have been studied.

Because the electrooxidation of PCM is often paralleled to the catalytically activated P450 oxidation in the liver [28], [29], electrochemical studies of PCM in aqueous solutions can prove to be an invaluable tool to gain deeper understanding on its toxicity in vivo. Moreover given the widespread usage of PCM, the topic of freshwater contamination is becoming especially important. The great majority of pharmaceutical drugs spillover in the environment tend to come either from wastewater and landfill leaching. This problem is exacerbated by the fact that many waste treatment facilities are not always capable of adequately removing its toxic degradation products [30]. Some of the treatment methods to remove PCM are (photo/electro) Fenton oxidation, activated charcoal, ultrafiltration and ozone oxidation [31]. It has been reported that its presence in water, or of its degradation products, can induce neurotoxic effects on aquatic organisms [32], inhibiting the enzyme acetylcholinesterase. Additionally, even if the concentration of this particular xenobiotic is relatively low, Elerssek *et al.* [33] have shown that the presence of other drugs with a similar mode of action can lead to synergistic interactions, increasing the risk of toxic effects. Consequently, given its role as freshwater pollutant, and its toxic effects on the liver in case of overdose the development of effective detection techniques is of paramount importance. In this regard, EC biosensors have shown significant promise on different fronts, both for PCM sensing in freshwater than in biological fluids. Their main advantage over traditional techniques such as HPLC, spectrophotometry, colourimetry and chemiluminescence is the ability to obtain a measurement via an in-line, cheap and rapid method [34]. In particular, the drastically lower cost can potentially allow hospitals that don't have access to expensive equipment to easily diagnose a case of suspected PCM overdose.

1.3 Nanomaterials as electrocatalysts for non enzymatic sensors

As anticipated in **Section 1.1** enzymatic biosensors are generally unstable and their catalytic activity is dependent on pH, temperature and ionic strength. In an effort to overcome these limitations non-enzymatic EC sensors have been developed. As the name suggests they do not employ an enzyme to induce an electrochemical change to be measured but are based on an electrocatalytic reaction happening on the working electrode surface. One of their main drawbacks are the limited specificity and fouling tendency where oxidation intermediates adsorb on the electrode surface and poison it. Anyhow, to improve the sensitivity of these devices the development of efficient catalysts is of fundamental importance. In the recent years nanomaterial-based electrochemical sensors have demonstrated to be powerful analytical tools [35], [36] and nanoparticles, nanosheets, nanowires, nanotubes have been extensively researched. Furthermore, multiple studies have now shown that a clear size dependence of the catalytic activity exists [37], [38] and that it may be ascribed briefly to surface and quantum effects. Accordingly, as the characteristic dimension d gets smaller, surface effects emerge

from the increasing proportion of uncoordinated atoms which are more unstable than bulk ones, thus more reactive towards other interacting species. Moreover, when d is lower than the exciton radius ($\approx nm$) quantum confinement leads to a splitting of the energy levels causing an increase in the HOMO-LUMO band gap. Noble metal nanoparticles, especially of Au, Ag and Pt in general show exceptional electrocatalytic behavior, decreasing overpotentials for relevant electrochemical reactions and even improving their reversibility [36]. For instance You *et al.* [39] reported a 170mV lower overpotential for the oxidation of H_2O_2 for a Pt nanoparticle modified electrode, compared to bulk Pt. Unfortunately the use of noble metals is usually prohibitive for many applications. For this reason, an interesting alternative is offered by metal oxides, which have shown promising results for the oxidation of aromatic compounds [40]. In particular, through the deliberate introduction of structure defects (e.g. substitutional atoms or oxygen vacancies in metal oxides) the electronic structure can be altered [41]. This in turn allows to regulate the energy of adsorption/desorption of the analyte with respect to the catalyst's surface. The Sabatier Principle states that the maximum catalytic activity occurs when binding energy is neither too strong, nor weak. Consequently, through accurate defect design significant improvements in the catalytic activity can be obtained.

1.4 Bismuth and bismuth related compounds

Bismuth, atomic number 83, can be described as a semimetal due to having electronic properties intermediate between metals and semiconductors [42]. It's characterized by a high carrier mobility, low effective mass, high magnetoresistance and relatively long mean free path [43]. Obtained as a byproduct of tin, lead or copper mining bismuth tends to be relatively inexpensive. Even though it's a heavy metal, like Pb, bismuth and its compounds are unusually safe and for this reason some authors have referred to it as a "green element" [44]. The main oxidation states of Bi are Bi(III) and Bi(V), where the former is the most common and stable of the two.

It's frequently used in the form of an oxide, halide, nitrate or as an oxo-halide.

In the field of heterogeneous catalysis Bi_2O_3 has been attracting considerable interest, given that its direct optical band gap is lower than TiO_2 (around 2.7eV - 2.5eV depending on the phase [45]). This difference with titania has been attributed to the different composition of their valence band. Accordingly the valence band of Bi_2O_3 is composed of the 6s lone pairs of Bi and the 2p of oxygen, whereas for TiO_2 it's comprised only of the 2p orbital of oxygen [46]. For this reason, the material has been considered as a promising photocatalyst for water splitting or pollutant degradation, possibly in combination with other phases so as to obtain better performing heterostructures [47]. Six different polymorphisms have been reported for Bi_2O_3 , and they are schematically shown in **Figure 1.4b**: (monoclinic- α , tetragonal- β , bcc- γ , and fcc- δ , triclinic- ω , orthorhombic- ϵ). At low temperature the stable phase is the monoclinic, pseudo orthorhombic $\alpha - Bi_2O_3$. However on heating at temperatures higher than 710°C, the α phase transforms into the cubic δ phase, in which only six of the eight anionic O^{-2} sites

per cell are occupied, making the structure highly defective. The stability interval of such a structure extends until the melting point at 824°C.

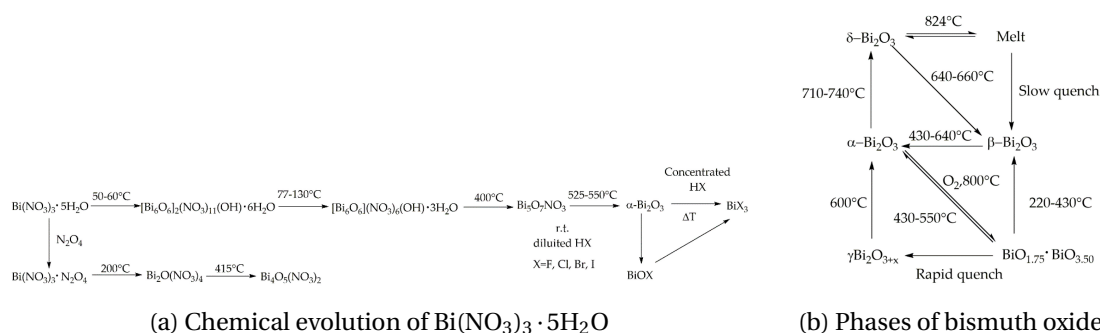


Figure 1.4 – Bismuth oxide phases and evolution of bismuth nitrate salt. Reproduced with permission from Bartoli *et al.* [48]

If a slow quench is performed from the melt the β phase can be obtained. The γ phase is usually quite unstable and difficult to synthesize without employing a proper support (metal or metal-oxide) [49]. Other metastable polymorphs are the triclinic $\omega - \text{Bi}_2\text{O}_3$ and the orthorhombic $\epsilon - \text{Bi}_2\text{O}_3$. Importantly, through controlled heating of bismuth nitrate it's possible to synthesize the bismuth subnitrate $\text{Bi}_5\text{O}_7\text{NO}_3$, as described in **Figure 1.4a**.

1.5 The aim of this research

Molecules such as PCM are attracting attention due to their toxicity at high concentrations and widespread use. For this reason a lot of effort has been put into trying to develop new and innovative materials that minimize the overpotential required to have electrooxidation. Consequently the main objective of this work is to first study the particular quantum mechanic interaction of PCM with a cluster of $\text{Bi}_5\text{O}_7\text{NO}_3$ and then to evaluate experimentally how and if a change in performance can be discerned from the progressive introduction of defects due to oxidation. This approach allows for a detailed insight onto the particular interaction of PCM on the bismuth cluster, while also setting a theoretical framework for the study of defect design. Kinetic studies are performed from a theoretical and experimental approach. Then they are compared with each other so as to determine if heterostructures of $\text{Bi}_2\text{O}_3/\text{Bi}_5\text{O}_7\text{NO}_3$ show superior catalytic behavior compared to their single-phase counterparts.

2 Theoretical Background

2.1 Electron transfer theories

Electron Transfer (ET) is an extremely common phenomenon, not only in physics but also in chemistry and biology. As suggested by the name, the process involves the transport of an electron by a species D, the donor, to a species A, the acceptor. One characterizes the ET event as **Outer Sphere** if the mechanism doesn't involve the forming or breaking of new bonds, or **Inner Sphere** if the electron transfer between the redox centers happens through a bridging ligand. The latter is usually seen in transition metal complexes, and very rarely in biological systems, since redox sites tend to be shielded by bulky proteins. In general outer sphere ET tends to be a less complex phenomenon and easier to study [50] : a first model had been theorized by Franck and Libby and subsequently improved by Marcus, whose treatment of the process was purely classical. For his work Marcus was awarded the Nobel Prize in Chemistry in 1992. Hopfield [51], and Levich and Doganadze have presented more elaborate quantum-mechanical models [52]. Before further treating the details of the aforementioned theories a few introductions are necessary.

Potential energy surface When considering ET processes one usually employs the concept of Potential Energy Surface (PES), particularly in the context of the Transition State Theory (TST). In such a theory it's assumed a quasi-equilibrium between the reactant and a transition state complex¹. Moreover, the notion of the PES plays a distinctively important role in the field of computational chemistry, allowing to link a particular geometrical configuration of a molecule with its energy [53]. In fact a PES is none other than a

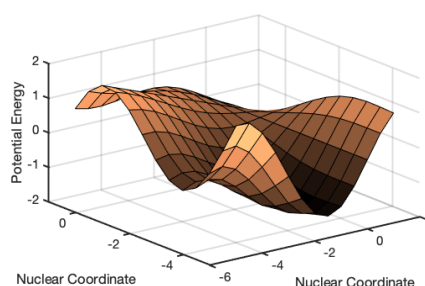


Figure 2.1 – Potential Energy Surface

¹Sometimes also called activated complex

multi-dimensional surface obtained by plotting the potential energy of the system as a function of a nuclear configuration coordinate Q , which has in itself the multiple geometrical degrees of freedom. Usually Q is made up of terms like bond lengths, bond angles, orientation or position of the reactants or even the solvent configuration, depending on which parameter is considered to be particularly relevant for the potential energy of the system.

Preliminary assumptions A PES such as defined above is only possible under the the *Born Oppenheimer approximation*, for which it is assumed that the nuclei are stationary relative to the electrons, justified by the fact that they have a mass that is three orders of magnitude heavier. Therefore, from a dynamical perspective it stands to reason that the electrons will move at a much higher speed, making the assumption in general acceptable. This allows to greatly simplify the application of the Schrödinger equation, separating the nuclear repulsion from the electronic energy. The electron can then be considered to be moving in a potential of immobile atoms in precise positions: this is sometimes called the adiabatic approximation. It is important to note that in the case of condensed matter such an approximation may not hold. Moreover, when considering an ET process it is usually reasonable to make another assumption, the so called Two State Approximation (TSA). According to this approach the mechanism of ET can be adequately described by two states: initial Ψ_i and final Ψ_f where the charge is localized respectively in the donor and acceptor sites. This means that a graph like the one shown below could be made where two PES relative to the reactant and product state intersect. This simplification too has its limits, particularly when a high density of electronic states are present in the initial and final state [54][55] (e.g. in the case of metal/semiconductor electrodes).

Adiabatic and Non-adiabatic states In **Figure 2.2** are shown the profiles of the PES for an adiabatic and a non-adiabatic process. It is instructive to note that each of these diagrams is relative to one system, where two parabolas^{II} can be distinguished: the one called R is relative to the state of the reactants, and P to the products. By that it's meant for example that when a representative point lies on the surface named R, the set of nuclear coordinates that describe the system would be in a configuration that resembles the reactants' state.

It has been proposed above that the curves R e P in **Figure 2.2** are parabolic and this is not a trivial assumption, so it's important to clarify that under such an approximation rests the idea that the vibrational modes can be modeled by an harmonic oscillator, obeying Hooke's Law. Nevertheless one must be careful when evaluating the molecular effect of polar solvents, since the reorientation of such molecules is strongly anharmonic, hence appropriate models must be used [56]. Finally, it is possible to give the following definitions:

" [...] when the system jumps from one solid "adiabatic" surface to the other on passing through the intersection region the process of jumping is called a

^{II}These not actual parabolas since the nuclear coordinates are multidimensional

"**nonadiabatic act**" [...]. When the probability of a chemical reaction occurring per passage is large (near unity) the reaction is, of course, called "**adiabatic**". In either case reaction can occur only if a system starting on the lower surface R finally goes over to P on the lower solid "adiabatic" surface [57]. "

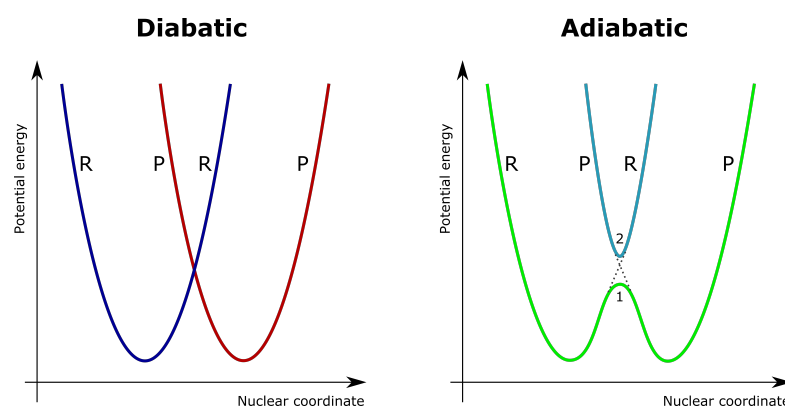


Figure 2.2 – Adiabatic and Non-adiabatic processes

Notably, an ET mechanism can be categorized as non-adiabatic if the interaction between the initial and final states is small, i.e. the electronic coupling^{III} V is close to zero. Consequently it's possible to consider the two states as independent, resulting in two diabatic surfaces. Alternatively when the coupling is strong, therefore V is big, the two adiabatic states repel each other and at the intersection between R and P a splitting occurs producing an upper and lower potential surface: it's supposed that the upper state is sufficiently high in energy not be thermally activated, as a result the system tends to rest on the lower one [58].

2.1.1 Libby Theory

As reported by Libby in 1952 [59] an important hypothesis was developed: the more the inner coordination shells of the donor and acceptor atom were similar the higher the rate of electron transfer between the two. Such an assertion was supported by the empirical evidence of the slowness of the $\text{Co}(\text{NH}_3)_6^{2+} - \text{Co}(\text{NH}_3)_6^{3+}$ exchange reaction, where in fact an important change in the Co-N bond length was required. The basis for this idea was "borrowed" in a way from spectroscopy: the Franck-Condon principle. Its IUPAC definition is the following:

" The Franck - Condon principle is the approximation that an electronic transition is most likely to occur without changes in the positions of the nuclei in the molecular entity and its environment. [...]"

In other words, the timescales for electronic transitions are profoundly smaller than those of the nuclear motions, therefore one can consider the atoms' position during an electron

^{III}Also known as Effective Charge Transfer Integral

transition as fixed. Hence, by analogy it was supposed that this would also be the case for ET processes. Therefore if an electron was to be transferred between to species, the reactants would find themselves in the wrong environment since the nuclei of the solvent molecules (or the coordination shells) couldn't have time to adapt to the electron jump, necessarily introducing an energy barrier.

2.1.2 Classical Marcus Theory

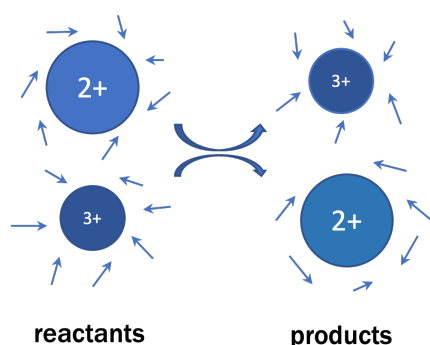


Figure 2.3 – Reactants and products with solvent

Libby intuition of the role played by the Franck-Condon principle during ET was correct, however it assumed that there would be a large difference in energy immediately before and after the ET. However, in the case of reactions occurring in the dark the law of energy conservation would evidently be violated, as astutely noted by Marcus, since the reagents would be in vibrational excited states and would eventually release energy. It was therefore postulated that fluctuations in the different nuclear coordinates had to occur (e.g. the orientation of the solvent molecules) and thanks to these fluctuations it would be possible to reach an isoenergetic configuration that satisfied the conservation of energy as well as the Franck-Condon principle.

Considering a profile of the PES of a system such as the one shown in **Figure 2.2 (a)** it is clear that the ET, according to Marcus' Theory, could occur only at the intersection between the PES of the reactants and the PES of the products, and this intersection is evidently a (N-1) dimensional surface if one assumes an N nuclear coordinates.

It is instructive to note that in the activated complex the solvent molecules are in a non-equilibrium configuration, and this is a direct consequence of the assumption of weak electron coupling underlying both Libby and Marcus models. This can be understood by considering that for a weak interaction as the reactants approach one another, if a suitable fluctuation in the solvent molecules happens, an activated complex can form. This activated complex will initially have the electron configuration of the reactants (state X) and then of the products (state X*), while maintaining the same atomic configuration. This means that the configuration of the solvent between X and X* is also same, but these states clearly differ in the charges of the reacting species, hence the average configuration of the solvent in the activated complex is not an equilibrium one. However if one considers a strong electronic interaction between the reactants, "the formation of one from the other would be very rapid and one need then not speak of them separately" [60], hence the above reasoning could not be made.

On the whole, Marcus theory describes a weakly coupled homogeneous outer-sphere ET and the physical model behind his approach to ET reactions chiefly considers the reacting species D and A as spheres with charges respectively Z_1 and Z_2 embedded in a solvent whose molecu-

larity is ignored and instead the dielectric continuum theory is being used. Furthermore it is supposed that the dielectric medium is unsaturated outside of the spheres A and D and that its response is purely linear. A schematic of the process is shown in **Figure 2.4**.

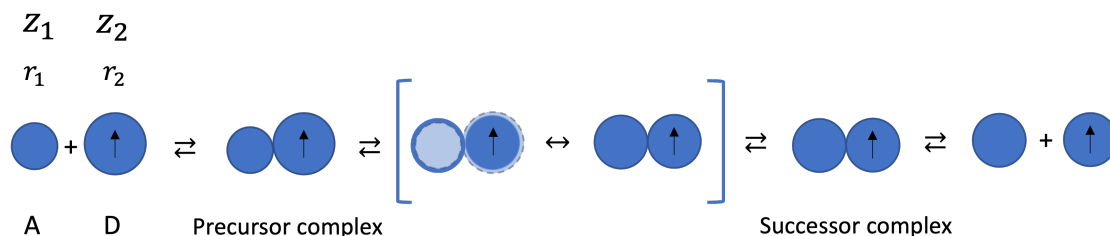


Figure 2.4 – Formation of the collision complex and subsequent electron transfer

As already anticipated in **Section 2.1** it is postulated that the atomic motions can be approximated by a harmonic oscillator model, therefore a quadratic dependence on the nuclear coordinates is to be expected. After a series of calculations, based on the minimization of energy and the Franck-Condon principle [61], Marcus derived an expression^{IV} for the activation energy for the collision complex

$$\Delta G^\ddagger = \frac{\lambda}{4} \left(1 + \frac{\Delta G^\circ}{\lambda} \right) \quad (2.1)$$

where ΔG° is the standard free energy of the reaction and λ is the reorganizational energy. This last term, λ is of great importance in the context of Marcus theory, and can be defined as the energy required to reorganize the nuclear coordinates so that the reactant state matches the configuration of the product state *before* the electron transfer actually occurs. It can be divided into two components:

$$\lambda = \lambda_i + \lambda_o \quad (2.2)$$

where λ_i is the inner shell component involving a change in bond angles/lengths change, and λ_o involving the reorganization of the surrounding solvent molecules.

In a model of spherical reactants, such as defined above, it's possible to give the following expression for λ_o :

$$\lambda_o = \frac{(\Delta e)^2}{2} \left(\frac{1}{a} + \frac{1}{b} - \frac{2}{R} \right) \left(\frac{1}{D_{op}} - \frac{1}{D_s} \right) \quad (2.3)$$

where a and b are the ionic radii of the reactants (including the coordination shell), R is their separation distance, D_{op} and D_s are the optical and static dielectric constants.

^{IV}In this formulation it's assumed that the electrostatic work to bring together the reactants to form the activation complex is zero

Furthermore the expression for λ_i can thus be given :

$$\lambda_i = \frac{1}{2} \sum (k_j (Q_j^r - Q_j^p)) \quad (2.4)$$

where Q_j^r and Q_j^p are the equilibrium normal mode coordinates for the j^{th} normal mode coordinate Q , and k_j is the force constant associated with it.

2.1.3 Generalized Marcus Theory

Tachiya in his 1993 paper [62] proposed a generalization of the classical Marcus theory. In his formulation he overcame the simplifying assumption of the solvent as a dielectric continuum, and developed a model which better accounts for its molecular nature. Accordingly, the local fluctuations of the electrostatic potential due to the oscillatory movement of the polar solvent molecules are taken in to consideration in terms of $\phi(\Delta V)$, which expresses the distribution of electrostatic potential difference between the acceptor and the donor.

The electron transfer will take place only if the potential difference passes through a precise value $e\Delta V^\ddagger$. An expression for it can be obtained by considering that in the initial state the interaction energy is zero^V and that for the electron transfer to occur the final state energy must coincide with the initial one:

$$e\Delta V^\ddagger = -IP + EA + \Delta g_s^e + \frac{e^2}{R} \quad (2.5)$$

where IP and EA are the ionization potential of the donor and the electron affinity of the acceptor, respectively. Δg_s^e represents the solvation energy of the produced ion pair due to the electronic polarization of the solvent. R stands for the distance between the interacting species, and e^2/R is the Coulomb attractive energy between the ion pair. The solvation energy can be expressed as follows[63]:

$$\Delta g_s^e = \frac{\Delta e^2}{2} \left(1 - \frac{1}{D_s}\right) \left(\frac{1}{a} + \frac{1}{b}\right) \quad (2.6)$$

where D_s , a and b have the same meaning as in expression 2.3.

Once a configuration that satisfies both the Franck-Condon principle and the conservation of energy is reached, the probability that the electron transfer process actually happens needs to be considered. According to the Landau-Zener theory [64] the probability that the electron will "hop" from the PES of the reactant state to the product state is given by:

$$P = 1 - e^{-\frac{2\pi J^2}{\hbar |\Delta \dot{E}|}} \quad (2.7)$$

^VAt least as a first approximation

where J is the electron coupling, which takes into account the interaction energy of the initial and final states. $\Delta\dot{E}$ is the difference of the time derivative of the potential energy. Finally, after approximating the expression 2.5 with a Taylor expansion^{VI}, and calculating the potential energy distribution, a formulation of the electron transfer rate is obtained:

$$k = \frac{2\pi}{\hbar} J^2 \frac{1}{\sqrt{4\pi k_B T \lambda}} e^{-\frac{(IP-EA-\Delta g_s^e - e^2/R)^2}{4k_B T \lambda}} \quad (2.8)$$

2.1.4 Generalized Mulliken Hush Theory

In the context of the TSA, an expression for the electron coupling J can be provided [65].

$$J = \frac{\mu_{12} \Delta E_{12}}{\sqrt{(\Delta\mu_{12})^2 + 4(\mu_{12})^2}} \quad (2.9)$$

Where μ_{12} is the dipole moment of the transition state, ΔE_{12} is the energy difference of the eigenstates involved and $\Delta\mu_{12}$ is the difference of dipole moments.

2.2 Semiempirical computational methods

Semiempirical computational methods are based on the Schrödinger equation, similarly to the *ab initio* methods, but with the substantial difference that empirical parameters are introduced to accelerate the calculations in a profound way, albeit at the cost of a reduced accuracy in the obtained results. Driven by the necessity to reduce computational complexity at a time where computers were dramatically less powerful than nowadays, the Simple Hückel method (Erich Hückel, ca. 1931) and the Extended Hückel Method [66] were developed. These methods allowed to model larger systems, and could be considered as a natural progression towards Self Consistent Field (SCF) semiempirical methods, which are the kind used in this study. The SCF procedure was first developed by Hartree by expressing an hypothetical polyelectronic wavefunction representative of the system as a product of single electron wavefunctions (the Hartree product):

$$\Psi_0 = \Psi_0(1) \cdot \Psi_0(2) \cdot \Psi_0(3) \dots \quad (2.10)$$

where Ψ_0 is a function of the coordinates of coordinates of the atom/molecule, $\Psi_0(1)$ is a function of the coordinates of electron 1, $\Psi_0(2)$ of electron 2, $\Psi_0(3)$ of electron 3, and so on... Having defined a "first guess" wavefunction, an iterative procedure is developed to refine its accuracy:

1. Solve the Schrödinger equation for the one electron wavefunction $\Psi_0(1)$ where the electron-electron repulsion component is expressed as a the repulsion between the

^{VI}Justified by the assumption of a nonadiabatic electron transfer

electron 1 and the mean electrostatic field of all the remaining electrons. The solution allows us to update $\Psi_0(1)$ to $\Psi_1(1)$.

2. Solve for $\Psi_0(2)$ moving in a field of $\Psi_1(1)$, $\Psi_0(3)\dots\Psi_0(n)$
3. Repeat for all single electron wavefunctions, and obtain Ψ_1
4. Repeat these last 3 steps for k cycles, until $\Psi_{k-1} \approx \Psi_k$

The main limitation of the Hartree product is not taking into account the electrons' spin and that being fermions they are antisymmetric with respect to exchange. For this reason the Slater wavefunction was developed, which differs from the Hartree product in that it's made up of spatial and spin orbitals and it's a determinant and not simply a product of wavefunctions. For the evolution to what is now known as the Hartree-Fock (HF) method, the *variational principle* played an instrumental role, and states that the expectation value of the energy operator is always greater (at most equal) to the ground state energy of the system. Consequently in the HF method, spin orbitals are optimized by minimizing their energy calculated with respect to the Slater determinant, giving rise to the Fock operator:

$$F_{rs} = H_{rs}^{core} + \sum_{t=1}^m \sum_{u=1}^m P_{tu} [(rs|tu) - \frac{1}{2}(ru|ts)] \quad (2.11)$$

Where H_{rs}^{core} is the hamiltonian relative to the core electrons, P_{tu} is the density matrix and $(rs|tu)$, $(ru|ts)$ are the two electron integrals. Notably H_{rs}^{core} depends only on nuclear coordinates and the basis set. The SCF procedure applied to the HF method requires having an initial guess of the coefficients to allow the calculation of the density matrix. Then, after the diagonalization of F its possible to calculate the corresponding P_{tu} . The process is repeated until adequate convergence is reached.

The main semiempirical methods are:

- **Parisier-Parr-Pople (PPP) method:** limited to π electrons, the Coulomb integral is treated as an empirical parameter, and the exchange integral and several two electron integrals are neglected. The overlap matrix is taken as unitary. Not used anymore.
- **Complete Neglect of Differential Overlap (CNDO):** not limited to π electrons like the (PPP) method. Similarly to the PPP the application of the zero differential overlap approximation means that the two electron integrals reduce to one and two center electron integrals. The core hamiltonian of different orbitals are considered proportional to the overlap integral.
- **Intermediate Neglect of Differential Overlap (INDO):** doesn't apply the zero differential overlap approximation to all atomic orbitals of the two-electron integrals, but only to the two-center electron integrals. More accurate the CNDO, but in general less than NDDO based methods.

- **Neglect of Diatomic Differential Overlap (NDDO):** The zero differential overlap approximation is not applied to orbitals of the same atom, hence a stark difference in accuracy compared to previous methods can be noted. To this category of semiempirical computational methods belong: MNDO, AM1, PM3 methods.

Limitations of the semiempirical methods The main limit of semiempirical methods is that given the implementation of empirical parameters their accuracy drastically drops whenever they are being used for molecules different than the ones used for the calculation of the parameters themselves. Moreover the errors in the calculation of energy levels can be profound, and difficult to predict and account for, since their magnitude can vary from case to case.

2.3 Theoretical principles of electrochemical sensors

As already introduced in **Section 1** biosensors can be classified on the basis of the transducer element used, giving rise to the following families: optical, mass based, or EC. Of particular interest in this work are the EC (bio)sensors. "Electrochemistry is the branch of chemistry concerned with the interrelation of electrical and chemical effects" [67], hence a change in electrical current (or potential) is evaluated to gain information regarding the nature of chemical reactions involved at the electrodes. Accordingly, EC sensing usually requires a three electrodes system: a Working Electrode (WE), a Reference Electrode (RE) and a Counter Electrode (CE) (**Figure 2.5**).

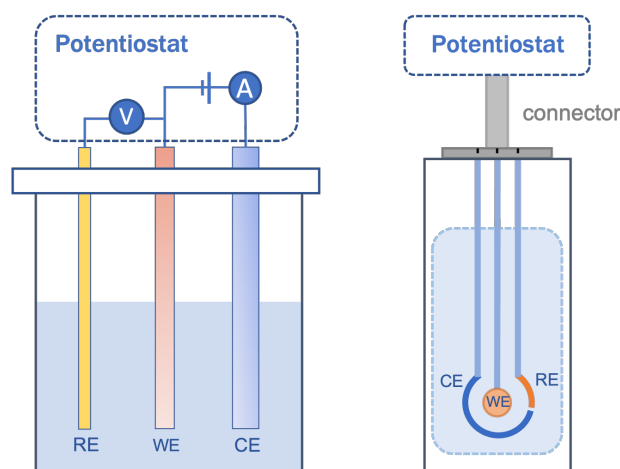


Figure 2.5 – Two types of three electrode systems

The WE for all intents and purposes is the transduction element of the system and the electrode where the (bio)chemical reaction of interest happens. However, to gain useful insight on the chemical reactions happening at the WE, it is necessary to have a precise knowledge of its electric potential E . Given that it's only possible to know a difference of E , a RE is employed, which is (ideally) unpolarizable, thus characterized by a well defined potential. Consequently, since the RE potential is fixed any changes in the cell can be intirely ascribed to the WE. The most common RE are: the *saturated calomel electrode* and the *silver silver chloride electrode*, though the internationally accepted reference electrodes are the Standard Hydrogen Electrode (SHE) and the Normal Hydrogen Electrode (NHE). An additional complication is the fact that when the potential of the WE is measured against a nonpolarizable RE, like Ag/AgCl, and a non-negligible current passes between the two, a voltage drop iR_s is also included in the measurement. Where R_s is the solution resistance between the electrodes. To overcome^{VII} this limitation, a counter electrode is introduced, such that most of the current is being passed between the WE and the CE. The latter must be characterized by a redox reaction on its surface sufficiently fast not to limit the one of interest happening at the WE, hence usually a good

^{VII}It should be noted that even in this configuration, there will always be some uncompensated resistance R_u , unless the RE is exactly on the surface of the WE, which would inevitably cause *shielding*

design strategy is to have a relatively large surface area [68]. Moreover it should not produce species by electrolysis that interfere with the WE.

Driving force behind electron transfer When in a three electrode system a potential difference is applied between the WE and the RE, given what has been said before, the electric potential on the WE alone is being changed. Moreover applying a precise electric potential on an electrode means controlling the Fermi level of its electrons, which is a measure of their mean electrochemical potential μ_e^S . Hence for a conductive electrode (supposed inert) in contact with a solution, the following condition for electrical equilibrium can be expressed:

$$E_F^M = E_F^S \quad (2.12)$$

Which is to say that the Fermi level of the two phases in contact must be equal.

Usually when an electrode is immersed in a solution the Fermi levels aren't aligned, hence to reach thermodynamic equilibrium and minimize the overall energy of the system electron transfer occurs (from the phase with the higher μ_e^S). With the use of a potentiostat the Fermi level of the electrode can be regulated such that oxidation or reduction reactions will be favoured.

2.3.1 Mass transfer and Fick's laws of diffusion

Mass transfer can be defined as the movement of matter from one location to another, and there are three main mechanisms by which it can be produced:

- *Diffusion*: movement of a material as a consequence of a concentration gradient
- *Migration*: movement of a charged species due to the effect of an electrical field
- *Convection*: movement of matter caused by stirring or hydrodynamic transport; it can be further classified into natural and forced convection

In general electrochemical systems such as the biosensors here under study tend to be designed in a way that allows to greatly simplify the mathematical treatment of the mass transport itself. Accordingly, the addition of an inert *supporting electrolyte* reduces to negligible levels the migrational component. Since it's being added in higher concentrations than the analyte, it's able to close the electrical circuit and at the same time increase the solution conductivity, thereby reducing the uncompensated solution resistance between the WE and the RE [69]. Convection instead can simply be removed by avoiding stirring and reducing to a minimum the vibrations in the cell. Given the above considerations, an approximate treatment of the mass transport can be presented in terms of Fick's first law of diffusion:

$$J = -D\nabla C(\vec{x}, t) \quad (2.13)$$

Where $C(\vec{x}, t)$ is the analyte concentration (either in the reduced or oxidized form). This expression describes the flux of species of interest as a function of the concentration gradient in space. Whereas Fick's second law of diffusion

$$\frac{\delta C}{\delta t} = D\Delta C(\vec{x}, t) \quad (2.14)$$

describes how the concentration changes with respect to time.

Additionally, given that the amount of species approaching the electrode will be proportional to the number of electron exchanged the following expression can be formulated:

$$J = \frac{i}{nFA} \quad (2.15)$$

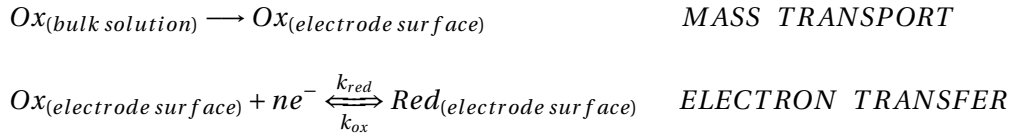
Which can be obtained by taking the time derivative of Faraday's law of electrolysis, and normalizing with respect to the electrode's surface A.

2.3.2 Reversibility and Nernst equation

Considering an electrode reaction not complicated by adsorption, homogeneous reactions or formation of phases, such as:



it can be described by the following scheme at least in the initial phase:



Whenever the rate of electron transfer is higher than the rate of mass transport the process can be defined as reversible, or nernstian: meaning it follows Nernst equation.

Nernst equation For an electron transfer process such as the one described by eq. 2.16 under equilibrium conditions it's possible to write:

$$E_{eq} = E^\circ + \frac{RT}{nF} \ln \frac{a_{Ox}}{a_{Red}} \quad (2.17)$$

Where E° is the standard potential of the redox couple, a_{Ox} and a_{Red} are the activities of the Ox and Red species. Because the activities tend to be unknown, it's easier to reformulate eq. 2.17 in terms of concentrations:

$$E_{eq} = E^\circ + \frac{RT}{nF} \ln \frac{\gamma_{Ox}}{\gamma_{Red}} + \frac{RT}{nF} \ln \frac{C_{Ox}^*}{C_{Red}^*} = E^{\circ'} + \frac{RT}{nF} \ln \frac{C_{Ox}^*}{C_{Red}^*} \quad (2.18)$$

Where γ is the activity coefficient, C^* is the concentration of the respective species in the bulk solution and $E^{\circ'}$ is the formal potential of the redox couple.

As a result of eq. 2.18 when $C_{Ox}^* = C_{Red}^*$ it's possible to write the following relationship:

$$E_{eq} = E^{\circ'}$$

2.3.3 Electrochemical kinetics and Butler-Volmer equation

For the simple electrode process described by eq. 2.16, the rate of reduction and oxidation reactions are respectively:

$$v_{Red} = k_{Red} \cdot C_{Ox}(0, t) = \frac{i_c}{nFA}$$

$$v_{Ox} = k_{Ox} \cdot C_{Red}(0, t) = \frac{i_a}{nFA}$$

Where $C(0, t)$ is the concentration of active species at the electrode surface, k_{Ox} and k_{red} are the rate constants of the two reactions, and i_c and i_a are respectively the cathodic and anodic currents.

Consequently the rate of the overall reaction is:

$$v_{Red} - v_{Ox} = k_{Red} \cdot C_{Ox}(0, t) - k_{Ox} \cdot C_{Red}(0, t) = \frac{1}{nFA} (i_c - i_a) \quad (2.19)$$

Now the rate constants can be approximated by the Arrhenius equation:

$$k_{Red} = k^{\circ} \frac{\alpha \cdot n \cdot F}{k^{\circ} \cdot e^{RT}} (E - E^{\circ'})$$

$$k_{Ox} = k^{\circ} \frac{(1 - \alpha) \cdot n \cdot F}{k^{\circ} \cdot e^{RT}} (E - E^{\circ'})$$

Where k° is the standard rate constant^{VIII}, n is the number of electrons that are being exchanged (per molecule), α is the transfer coefficient^{IX} ($0 < \alpha < 1$).

An important consequence of the above expressions is the fact that even if an active species has a low *intrinsic ability* to exchange electrons, it's possible make the process more kinetically favourable by increasing the overpotential η , where $\eta = (E - E^{\circ'})$.

Finally, after substituting the Arrhenius form of the rate constants in eq. 2.19 and reorganizing

^{VIII}The standard rate constant can be interpreted as a measure of the intrinsic tendency of a species to participate in an electron transfer process

^{IX}The transfer coefficient α takes into account how symmetric (or not) is the energy barrier associated to a redox half-reaction

the expression, the Butler-Volmer equation can be obtained:

$$i = i_c - i_a = nFAk^{\circ} \cdot \left[C_{Ox}(0, t) \cdot e^{-\frac{\alpha \cdot n \cdot F}{RT} (E - E^{\circ'})} - C_{Red}(0, t) \cdot e^{\frac{(1-\alpha) \cdot n \cdot F}{RT} (E - E^{\circ'})} \right] \quad (2.20)$$

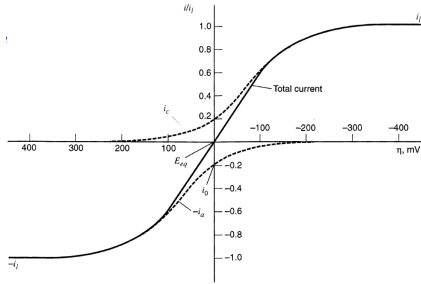


Figure 2.6 – Current-overpotential relationship according to BV theory

Another formulation of **eq. 2.20** is possible, simply derived by dividing by i_0^X , allowing to express the current signal as a function of the overpotential η instead of the formal potential:

$$i = i_0 \left[\frac{C_{Ox}(0, t)}{C_{Ox}^*} \cdot e^{-\frac{\alpha n F \eta}{RT}} - \frac{C_{Red}(0, t)}{C_{Red}^*} \cdot e^{\frac{(1-\alpha) n F \eta}{RT}} \right]$$

Figure 2.6 expresses graphically how the current changes with respect to η according to Butler Volmer theory. The main consequence of this mathematical description of the faradaic current is that the condition of equilibrium where $i = 0$ should be intended in a dynamical way, where i_a and i_c are balanced.

Butler Volmer under equilibrium conditions To have confirmation of the validity of the Butler-Volmer kinetic theory it must agree with the results obtained by thermodynamic considerations under the condition of equilibrium.

When the electric potential of the electrode is at the equilibrium value E_{eq} the cathodic and anodic current will equal each other so that the net (faradaic) current will be zero.

Hence from eq. 2.20:

$$nFAk^{\circ} \cdot C_{Ox}(0, t) \cdot e^{-\frac{\alpha \cdot n \cdot F}{RT} (E - E^{\circ'})} = nFAk^{\circ} \cdot C_{Red}(0, t) \cdot e^{\frac{(1-\alpha) \cdot n \cdot F}{RT} (E - E^{\circ'})}$$

that gives:

$$\frac{C_{Ox}}{C_{Red}} = e^{\frac{n \cdot F}{RT} (E_{eq} - E^{\circ'})}$$

Knowing that at equilibrium the concentration of the active species at the surface C equals the one in the bulk C^* we can write:

$$\frac{C_{Ox}^*}{C_{Red}^*} = e^{\frac{n \cdot F}{RT} (E_{eq} - E^{\circ'})}$$

And then by taking the natural logarithm at both sides of the equation the familiar Nernst equation (see 2.17) can be obtained.

^XWhere $i_0 = F A k_0 C$ is the exchange current

2.3.4 Cyclic Voltammetry

Cyclic Voltammetry (CV) is a type of voltammetry technique: this means that a change in the potential is induced to the WE, and the current response is observed. Its ease of use and versatility makes it one of the most extensively employed techniques for the study of electroactive species, in fields such as biochemistry, electrochemistry, organic and inorganic chemistry [69]–[71].

Fundamentals CV consists in sweeping linearly the potential of the WE from an initial potential E_i to E_f , and then again from E_f to E_i , thus completing a cycle (see **Figure 2.7b**). At the same time the value of the produced current as a result of the departure from equilibrium imposed by the potentiostat is measured. Care should be taken not to stir or agitate the solution, so that a purely diffusive mass transport can be assumed.

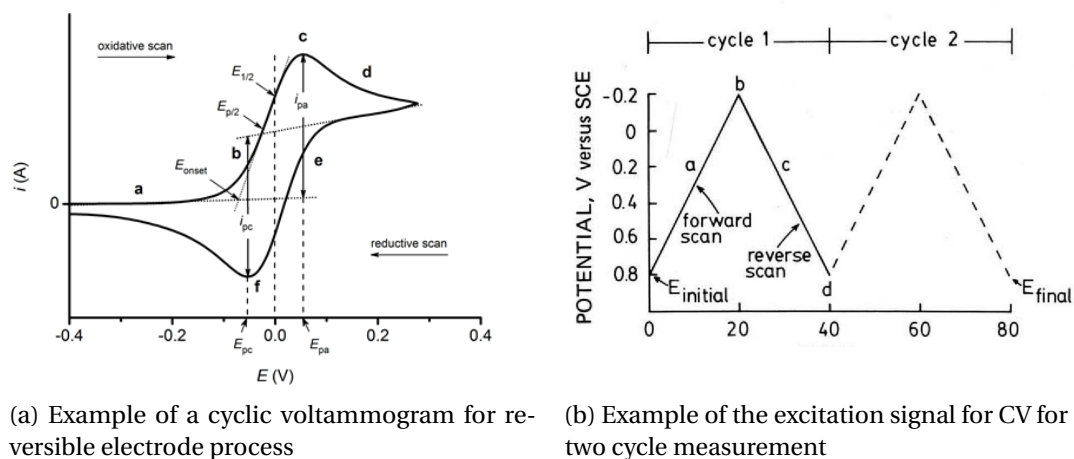


Figure 2.7 – Cyclic voltammogram and excitation signal

After the measurement is complete, a graph like the one shown in **Figure 2.7a** is produced (represented with respect to the US convention), where the applied potential is on horizontal axis and the current on the vertical axis. It should be noted that the shape of the proposed example graph is relative to a reversible electrode process, which as already said means that the mass transport is the rate determining step. Assuming that initially only oxidized species (Ox) are present: in the forward scan, as the potential is swept to more negative E , when the potential reaches a point where the reduction of Ox is possible the concentration of C_{Ox} decreases to a value imposed by 2.17, relatively to the bulk solution concentration. Consequently a diffusion gradient is produced, hence from 2.13 a mass flux is induced and a current begins to flow. Moreover since E is not maintained constant but swept linearly, the aforementioned concentration gradient is progressively increasing, until $C_{Ox}(0, t) = 0$. After this point the gradient diminishes and the diffusion later increases in thickness: as a consequence the current decreases. Once the scan is reversed, an analogous situation is presented, albeit with main

reaction on the electrode being the oxidation of the reduced species (Red) produced in the forward scan.

Reversible processes and Randles-Ševčík equation

A quantitative description of the above discussion for reversible processes is provided by 2.14, where its one-dimensional formulation is:

$$\begin{cases} \frac{\delta C_{Ox}(x,t)}{\delta t} = D_{Ox} \frac{\delta^2 C_{Ox}(x,t)}{\delta x^2} \\ \frac{\delta C_{Red}(x,t)}{\delta t} = D_{Red} \frac{\delta^2 C_{Red}(x,t)}{\delta x^2} \end{cases}$$

Given the following boundary conditions:

$$\begin{cases} C_{Ox}(x,0) = C_{Ox}^* \\ C_{Red}(x,0) = 0 \\ C_{Ox}(x \rightarrow \infty, t) = C_{Ox}^* \\ C_{Red}(x \rightarrow \infty, t) = 0 \\ J_{Ox}(0, t) = -D_{Ox} \left. \frac{\delta C_{Ox}(x,t)}{\delta x} \right|_{x=0} = \frac{i}{nFA} \\ J_{Ox}(0, t) = -J_{Red}(0, t) \end{cases} \quad (\text{If the process is reversible})$$

To these conditions it's also necessary to add the time-potential relationships:

$$\begin{cases} 0 < t < t_r & E = E_i - v \cdot t \\ t > t_r & E = E_i - 2 \cdot v \cdot t_r + v \cdot t \end{cases}$$

Where t_r is the time after which the scan is reversed, E_i is the initial potential and v the scan rate. For a planar electrode the peak current can be obtained by applying the Laplace transform to the differential equations defined above:

$$i_p = 0.4463 \cdot n \cdot F \cdot A \cdot C_{Ox}^* \cdot \left(\frac{nFvD_{Ox}}{RT} \right)^{\frac{1}{2}} \quad (2.21)$$

Where n is the number of electrons exchanged in the process, and the other symbols have their usual meaning. This expression, called *Randles-Ševčík equation*, applies not only to the cathodic peak but also to the anodic one as well. Furthermore it's frequently used to estimate the diffusion coefficient of electroactive species, or the electroactive area [72]–[75]. Notably, from eq. 2.21 for a reversible electrochemical process plotting i_p vs \sqrt{v} gives a linear dependence, where the increase in current as a consequence of a faster scan rate v can be related to the reduced thickness of the diffused layer, hence a greater concentration gradient.

Relevant properties of reversible processes	
Peak-to-peak separation (at 25°C)	$\Delta E_p = 59/n$
Ratio of forward and backward peak current	$i_{pf}/i_{pb} = 1$
Peak forward current and scan rate	$i_{pf}/\sqrt{v} = const$
Formal potential (for $D_{Ox} = D_{Red}$)	$E^{\circ'} = (E_{pf} + E_{pb})/2$

Table 2.1 – Useful properties of reversible processes

Degree of irreversibility, adsorption and Laviron equation

An electrode process is irreversible when the electron transfer is the rate determining step, as opposed to mass transfer in reversible processes. Furthermore, this kind of electrochemical behavior from a chemical standpoint is usually associated with a reaction on the electrode surface that as a result of the electron transfer causes a transformation into a different species. Moreover, even considering a reversible process, as the scan rate is increased it tends to be more and more irreversible: when in this intermediate state it's called quasi-reversible.

Laviron equation To determine the transfer coefficient and the rate constant of an electrode process where the oxidized and reduced species tend to be adsorbed at the electrode surface, the mathematical treatment of Laviron [76] can be a powerful tool. It concerns diffusionless systems, thus systems where diffusion effects are not taken into consideration in the development of the model, and its applicability ranges from reversible to completely irreversible processes. If a Langmuir isotherm is obeyed, the current can be described by a dimensionless function ψ and it's possible to take a limited form of this expression if the following experimental condition is fulfilled :

$$\Delta E_p > \frac{200}{n} mV$$

Hence the peak potentials E_p can be described by:

$$\begin{cases} E_{pc} = E^{\circ'} - (RT/\alpha nF) \cdot \ln[\alpha/m] \\ E_{pa} = E^{\circ'} - [RT/(1-\alpha)nF] \cdot \ln[(1-\alpha)/m] \end{cases} \quad (2.22)$$

Where $m = (RT/F)(k_s/nv)$, k_s the rate constant of the electrochemical reaction.

The value of the transfer coefficient α is calculated by plotting the anodic and cathodic potential as a function of the (base 10) logarithm of the scan rate: the obtained slopes of the two

fitting curves are equated to the ones given by **eq. 2.22**: $2.3RT/(1-\alpha)nF$ for the anodic peak, $-2.3RT/\alpha nF$ for the cathodic peak.

The rate constant can be calculated with the use of:

$$\log(k) = \alpha \log(1-\alpha) + (1-\alpha) \log \alpha - \log(RT/nFv) - \alpha(1-\alpha)nF\Delta E_p/2.3RT \quad (2.23)$$

3 Materials and Methods

3.1 Computational study

On simulating the oxidation of paracetamol on a bismuth functionalized carbon electrode a few assumptions were necessarily made. Firstly on account of the oxidation process itself: a direct electron transfer mechanism is considered as opposed to an intermediate-mediated one. Secondly on calculating the electron transfer rate constant the following approximations were made:

- The electron transfer is solely outer-sphere, therefore bridging ligands are absent
- The paracetamol molecule on approaching the Bi cluster loses its hydration shell
- The process is treated as a homogeneous electron transfer

After the geometry of the bismuth cluster and the paracetamol were independently optimized (see Section 3.1.1 and 3.1.2), two fictitious bonds were created between two carbon atoms of the aromatic ring of paracetamol and two bismuth atoms on the cluster. This constraint even though not physically meaningful helps the optimization of the system. Subsequently five water molecules were added and positioned near the paracetamol molecule, making sure that none was between the cluster and the paracetamol itself. The chosen number of water molecules was considered the minimum number to give rise to an adequate amount of hydrogen bonds without excessively complicating the system. Finally a Molecular Mechanics optimization was done, followed by a semi-empirical one. Then the fictitious bonds were broken and a single point calculation was done to obtain the necessary values to include in the generalized Marcus equation.

3.1.1 Bismuth cluster

The obtained crystal structure of $\text{Bi}_5\text{O}_7\text{NO}_3$ is based on the work of Ziegler et al [77]. From the nuclear coordinates a *.cif* file was produced with Mercury[®]. The standard unit cell of

$\text{Bi}_5\text{O}_7\text{NO}_3$ is made up of 64 atoms, which is not computationally treatable on a standard PC. Hence, to simplify the model a 15 atom asymmetric cell was exported as a *.mol* file. Through Avogadro[®] a few modifications to the cell were made, namely the bonding of hydroxyl groups to the Bi atoms which as a result of the simplification of the cell became undervalent. This also had the positive result of better estimating the heterogeneous nature of the synthesized bismuth oxynitrate. Notably, the presence of Bi_2O_3 and OH groups on the surface is to be expected [78]. This is mainly due to the high reactivity of under-coordinated atoms on the surface of the nanoparticles, and the direct exposure to O_2 and H_2O present in the air. After a rough definition of the cluster, the *.mol* file was imported in Hyperchem[®]. Firstly, a Molecular Mechanics simulation was run. This step is not necessary but it allows to reach convergence faster. The geometry optimization was stopped at 0.01. Then a semi-empirical simulation with PM3 as method was done, and again interrupted when convergence reached 0.01. Hence a minimum in energy was obtained, and the nuclear disposition is shown in **Figure 3.1**. It's important to emphasize that it's very difficult to say for sure if it's an absolute minimum. Another important point to highlight is that since bismuth has an atomic number of 83, there are a great number of electrons making up its electronic shells. However, at the same time semi-empirical methods like PM3 are based on the Hartree-Fock approximation. This means that electronic interactions are neglected, causing an imprecise description of the electronic bands [79]. A better alternative is to make a DFT simulation, however much more computationally demanding.

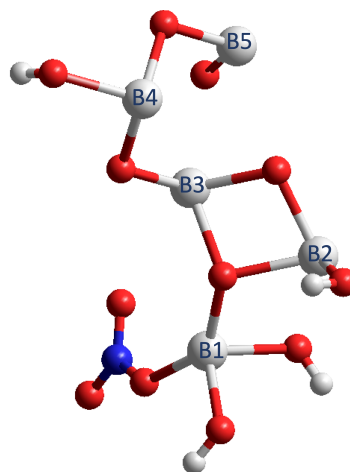


Figure 3.1 – Cluster of $\text{Bi}_5\text{O}_7\text{NO}_3$

3.1.2 Paracetamol

The chemical structure of the molecule of Paracetamol was drawn using ChemDraw[®]. Afterwards inside Hyperchem[®] a Molecular Mechanics geometry optimization was done, followed by a semi-empirical PM3 simulation. The configuration reached at convergence is shown in **Figure 3.2**.

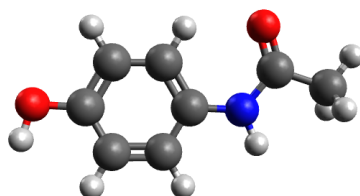


Figure 3.2 – Optimized molecule of Paracetamol

3.2 Materials synthesis



Figure 3.3 – Example of a sample obtained after calcination

All materials were purchased from Sigma Aldrich (US), unless otherwise stated.

Inspired by the works of Kodama [80] and Gadhi *et al* [78] heterostructures of Bi_2O_3 and $\text{Bi}_5\text{O}_7\text{NO}_3$ were produced via a simple solid state method using as a precursor salt $\text{Bi}(\text{NO}_3)_3 \cdot 5\text{H}_2\text{O}$. A total of 9 samples were synthesized at different calcination temperatures, as shown in Table 3.1. The only difference in the synthesis of the produced samples is the calcination temperature of the last step, that will influence the relative proportion of the phases making up the heterostructure. Firstly, the precursor salt ground with a pestle and mortar was heated and kept at $200\text{ }^\circ\text{C}$ for one hour to obtain a complete dehydration. Then, as a second

step the temperature was raised to $300\text{ }^\circ\text{C}$ and maintained for two hours. In the last step of the process the temperature is kept between $400\text{ }^\circ\text{C}$ and $600\text{ }^\circ\text{C}$, depending on the samples. Finally the cooling of the samples is done in air. It should be noted that all of the calcinations are done in a partial atmosphere of N_2 to better control the tendency of the bismuth nitrate to oxidize. Moreover the heating ramp was set to $10\text{ }^\circ\text{C}/\text{min}$ for all steps.

	Dehydration (1h)	Second step (2h)	Third step (1h)
B400	$200\text{ }^\circ\text{C}$	$300\text{ }^\circ\text{C}$	$400\text{ }^\circ\text{C}$
B425	$200\text{ }^\circ\text{C}$	$300\text{ }^\circ\text{C}$	$425\text{ }^\circ\text{C}$
B450	$200\text{ }^\circ\text{C}$	$300\text{ }^\circ\text{C}$	$450\text{ }^\circ\text{C}$
B475	$200\text{ }^\circ\text{C}$	$300\text{ }^\circ\text{C}$	$475\text{ }^\circ\text{C}$
B500	$200\text{ }^\circ\text{C}$	$300\text{ }^\circ\text{C}$	$500\text{ }^\circ\text{C}$
B525	$200\text{ }^\circ\text{C}$	$300\text{ }^\circ\text{C}$	$525\text{ }^\circ\text{C}$
B550	$200\text{ }^\circ\text{C}$	$300\text{ }^\circ\text{C}$	$550\text{ }^\circ\text{C}$
B575	$200\text{ }^\circ\text{C}$	$300\text{ }^\circ\text{C}$	$575\text{ }^\circ\text{C}$
B600	$200\text{ }^\circ\text{C}$	$300\text{ }^\circ\text{C}$	$600\text{ }^\circ\text{C}$

Table 3.1 – Calcination temperatures of the different samples

3.3 Screen printed electrode functionalization

To functionalize the working electrode of the SPE from Dropsens[®] a drop casting procedure was employed. Such a deposition method has the advantage of being simple and not requiring complex and expensive instruments to perform. However it should be noted that in the literature a few limitations have been highlighted [81], such as the coffee ring effect. Thus a

truly uniform deposition is not easily attainable, and for applications in electrocatalysis this could mean non-reproducible results. In order to improve the quality of the coverage the quantity of liquid on the drop was calibrated so that the contact angle was approximately not over 90° , and the drop maintained heated to increase the inward Marangoni flow (though of limited intensity compared to organic solvents). Moreover, to facilitate the comparison with the work of Madagalam *et al.* [82] the same molar concentrations for the aqueous dispersions were used. That is 12mg synthesized materials in 4ml of DI water. The dispersions were thus sonicated until homogeneous, and then through the use of an air driven micropipette (1-5 μ L) precisely 5 μ L were deposited on the working electrode surface with the help of an optical microscope (as shown in **Figure 3.4**). Since the area of the working electrode is 0.12cm² the coverage turns out to be 41.7 μ L/cm². Meaning that for each deposition a total of $1.25 \cdot 10^{-7}$ mg of material are covering the electrode's surface. For all samples the sonication was performed with the use of a sonicator bath, except for B600, which was tip sonicated because of its low solubility.

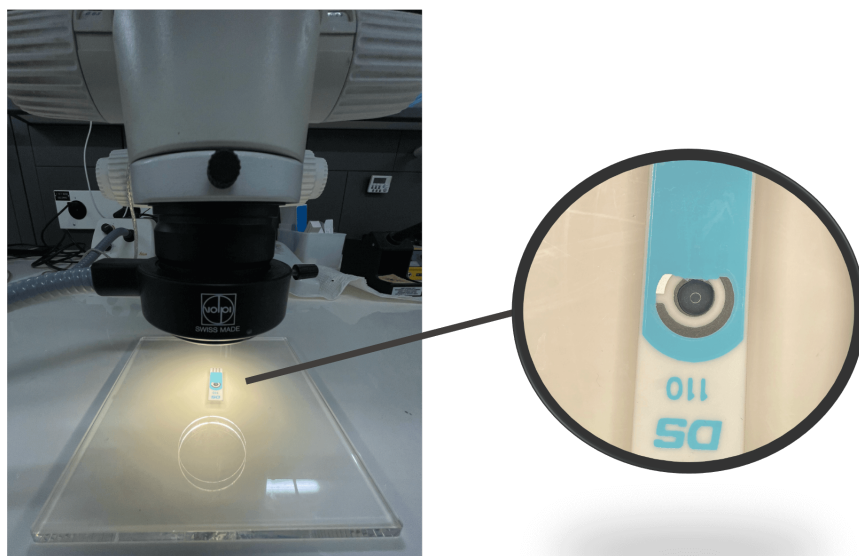


Figure 3.4 – Drop casting setup with the help of an optical microscope

After the deposition was performed the sensors were placed in an oven at 35 °C and kept inside until full evaporation. Particular care was put into making sure that while moving the sensor from the microscope to the oven the drop didn't expand to the reference and counter electrodes. In fact, a contamination of the counter electrode could likely mean a reduced electrical conductivity, even though having a much larger area than the Working Electrode this is likely not be particularly problematic. A more serious issue is the contamination of the Reference Electrode which in the best case would translate in a constant shift in the potential peaks during cyclic voltammetry, at worst it could mean that not even a delta in potential could be applied with precision during the measurement.

3.4 Cyclic voltammetry analysis parameters

The CV analysis was performed on an Autolab Potentiostat where every time a measurement was made the program would first turn on the cell then apply 0 V for 5 seconds to reach a stable state and then run the actual experiment with a cyclic potential being applied. The defined parameters of the experiment are described in **Table 3.2**. It should be noted that the scan rate was varied between 0.05 V/s to 0.3 V/s in steps of 0.05 V/s when the kinetic behavior of the sensor was the subject of study. However for the determination of the calibration curves multiple CV were performed at 0.1 V/s at different concentrations of Paracetamol in 0.1M of PBS. For each measurement 3 scans were done: this is to guarantee that a relatively stable state is obtained. Moreover each CV was done on 100 μ L of PCM solution dropped on the WE surface with the help of a pipette.

Start potential	0 V
Upper vertex potential	0.9 V
Lower vertex potential	-0.3 V
Stop potential	0 V
Number of scans	3
Scan rate	from 0.05 V/s to 0.3 V/s in steps of 0.05 V/s

Table 3.2 – Setting parameters for the Cyclic Voltammetry analysis

3.5 PBS and PCM solutions preparation

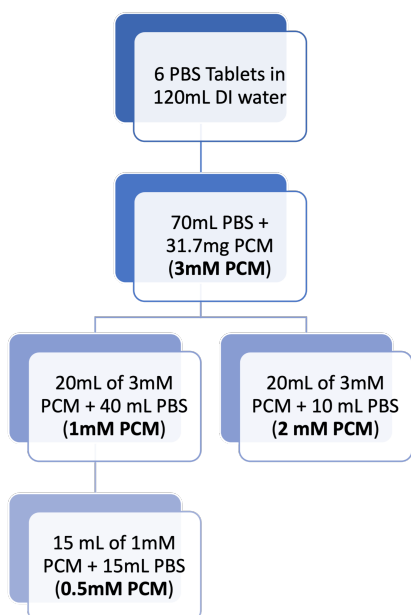


Figure 3.5 – Preparation procedure for the different concentrations of PCM + PBS

To guarantee reproducible results a standardized preparation procedure for the solution of PCM was devised. Firstly 120mL of PBS were prepared by dissolving 6 commercial tablets of PBS in 120mL of DI water, facilitated by the use of a sonicator bath. Consequently a 0.1M of PBS was obtained, of which 70mL were then combined with 31.7mg of PCM to get a 3mM solution of PCM. After that, through successive dilutions solutions of 0.5mM, 1mM and 2mM were produced. Because the CV at different scan rates for the functionalized sensors were always performed at a concentration of 1mM of PCM, the preparation procedure considered a 50% higher volume for this particular concentration. Moreover, to avoid the risk of analysing degradation products of PCM the obtained solutions should be discarded after two weeks outside of a fridge.

3.6 Carbon paper-based electrochemical cell for preliminary test

3.6.1 Carbon paper functionalization

To perform a preliminary test of the produced materials in **Section 3.2** and to evaluate their interaction with the carbon paper surface an ad hoc dispersion was devised. The materials were dispersed in ethyl alcohol with a 1% of butanol in the same concentration as for the SPE, that is 3 mg/ml. The addition of butanol, having a higher boiling temperature, helps to avoid the formation of large aggregates. Given the relatively low solubility of the synthesized heterostructures, to avoid precipitation when mixed with the alcoholic solution an ultrasonic bath was employed. Once an acceptable dispersion was obtained, with the help of a pipette 210 μL were deposited on a 1x5cm strip of carbon paper. In this way approximately the same amount of particles as with the SPE were deposited. The choice of depositing on strips instead of electrodes already cut to size was due to the difficulty of their transportation from the Polytechnic of Turin to the EPFL Laboratories in Neuchâtel. Subsequently the carbon paper strips were calcined at 300 ° C for 30 min in an inert atmosphere (N_2), to stabilize the deposition while avoiding unwanted oxidation.

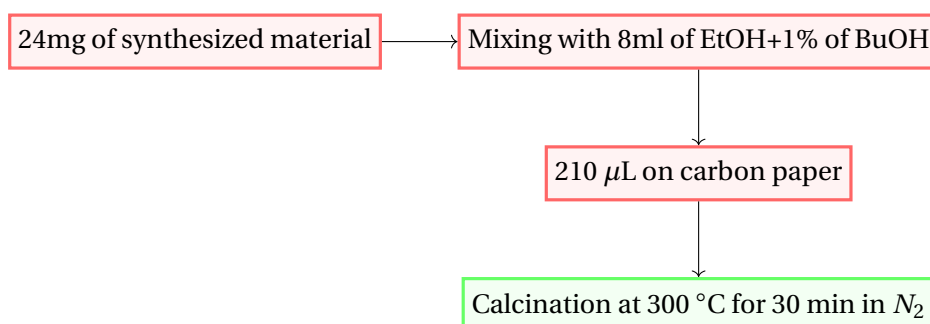


Figure 3.6 – Flowchart of the deposition process

3.6.2 Carbon paper-based working electrode fabrication

With the aim of performing a preliminary test of the performance of the synthesized materials the functionalized carbon paper described in **Section 3.6.1** was used as a Working Electrode. For this reason it was cut to size so to be composed of a square of approximately 4mm x 4mm with a rectangular strip 12mm x 3mm acting as a conductive pad for the electrical connection to the potentiostat (See **Figure 3.7**). Only the square is to be immersed in the electrolytic solution. However to ensure reproducibility during measurements it was necessary to support the C-paper in a stable matter. Accordingly for each produced electrode a 15mm x 5mm plastic (PS) support was cut from a larger piece. A thin layer of epoxy resin was deposited on the plastic support through the use of a toothpick, and afterwards the carbon paper placed on top of it. The obtained supported electrode was thus left to stabilize overnight.

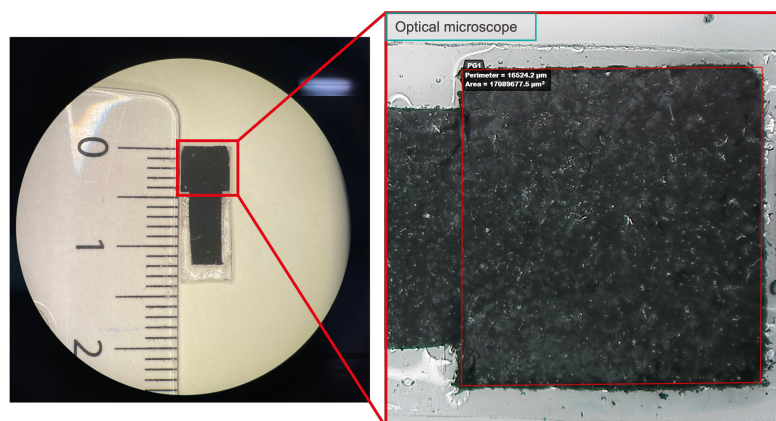


Figure 3.7 – Carbon paper-based working electrode under optical microscope for the measurement of its area

3.6.3 Electrochemical cell assembly

After the WE based on supported carbon paper was produced as described in **Section 3.6.2** an electrochemical cell was to be set up. Given the need to control accurately the immersion of the WE in the electrolytic solution a screw-operated moving base was used. The RE was a Ag/AgCl electrode and the CE a platinum foil electrode.

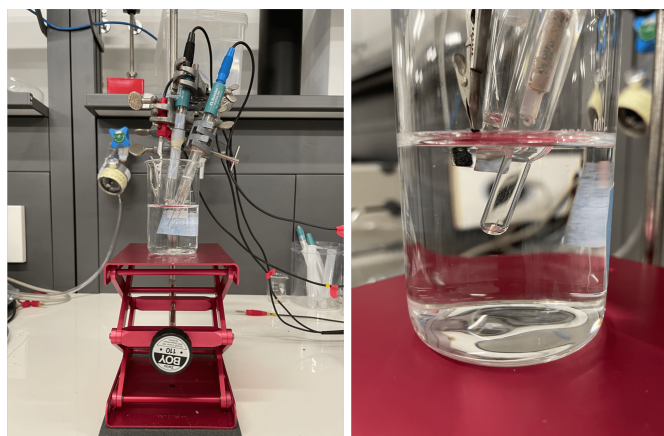


Figure 3.8 – Electrochemical cell setup

3.7 Paper-supported electrochemical sensor fabrication

To produce a prototype of a paper supported electrochemical sensor a first draft was done on paper to evaluate the relative distances between the conductive lines, and the general dimension of the sensor itself. After that a first test was performed with the use of a plastic stencil obtained. However this kind of system without adequate clamping leaves some space

between the deposition support and the stencil that causes smudges and imperfections in the printing procedure. Because the aim of this study is not necessarily to propose a commercial methodology for the fabrication of paper based sensors, but just to evaluate their feasibility a lab-based approach for prototyping is employed.

First of all the paper support chosen was common office paper (Navigator Universal). Which compared with Whatman filter paper commonly proposed in the literature has better mechanical properties and allows to limit the electrochemical reaction to happen mainly on the top side of the paper itself. This can be ascribed mainly to its lower permeability. With the help of common adhesive paper a pattern is defined by not covering the areas where the deposition has to take place: a mask is in effect created. Then silver paste is spread with the help of a spatula, acting in the same way of a squeegee in a common screen printing method. By removing the adhesive tape conductive lines of silver are created, which need to be stabilized to allow the epoxy-based binder to cross-link and the silver particles to sinterize, and thus create a percolating path for the electric current. For this reason the paper with the silver paste was kept in the oven at 80 °C for three hours. After that carbon paste was deposited on a conductive silver line to create the CE, and on the adjacent line to allow a stable support for the carbon paper acting as a WE. Then epoxy resin is spread to create an hydrophobic barrier confining the electrolytic solution to a precise zone and most importantly to avoid the that the silver lines at the CE and WE come into contact with the solution. This is because silver gives very strong peaks in the potential range used in our CV experiments. In conclusion a final heat treatment is performed to stabilize the carbon paper and allow the cross-linking of the epoxy resin, at 80C for one hour. The RE is simply composed of a longer silver line, left exposed.

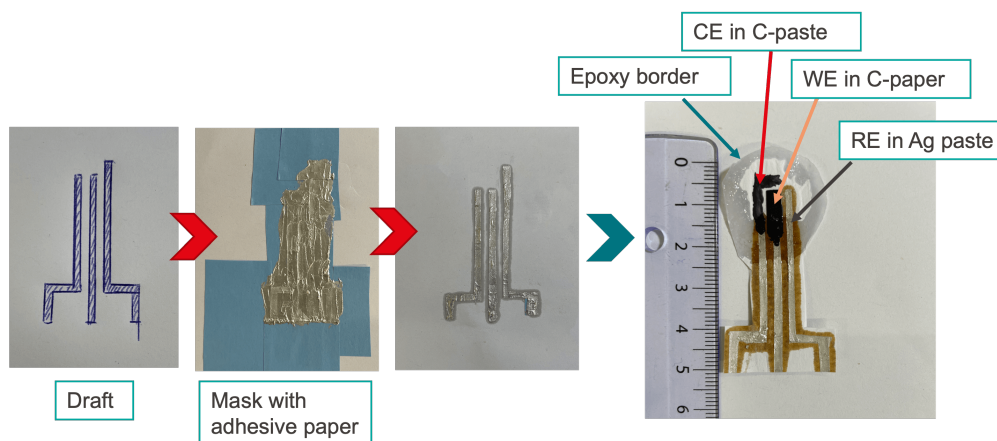


Figure 3.9 – Paper-supported electrochemical sensor

4 Results and Discussion

4.1 Computational model

In Figure 4.1 the optimized structure of the $\text{Bi}_5\text{O}_7\text{NO}_3$ cluster is presented, and for clarity the fictitious bonds are also indicated (even though, as already anticipated in Section 3.1, they were removed in the last step of the computational process). This configuration was the only one that reached the required (though arbitrary) energy convergence of 0.01. The other ones, indicated in **Figure 4.2** showed instead a marked instability. Moreover it should be noted that in this study it was considered as "rejected" any configuration that:

- Reached convergence but with a distance between the π electrons of the aromatic ring of paracetamol and the adjacent bismuth atoms of the cluster was over 4Å. A good first approximation was determined to be the length of the fictitious bonds which were previously set up to help with the molecular mechanics optimization.
- Didn't reach the required convergence of 0.01.

The reasoning behind this selection methodology of the different configurations obtained during the computational modeling of the system was multifold. The objective was to try to get the most energetically stable and kinetically favourable configuration for the electron transfer. Hence the need for convergence of the calculated energy was to make sure that a minimum could be reached, even though it is widely accepted that saddle points in the PES could easily be mistaken for minimum. Given the Boltzmann distribution function the minima of the PES are the most populated states of the system, thus the set of nuclear coordinates obtained are potentially descriptive of the most probable state of the system, at least in a non excited configuration. Moreover, given **Eq. 2.1**, the rate constant of electron transfer is inversely proportional to the distance between the centers of the reactants, hence the chosen configuration was the one that minimized that distance. It's clear that for relatively isoenergetic configurations, from a kinetic point of view, if one is such that the electron transfer is favoured, that configuration will prevail. A good analogy for this situation could be modeled

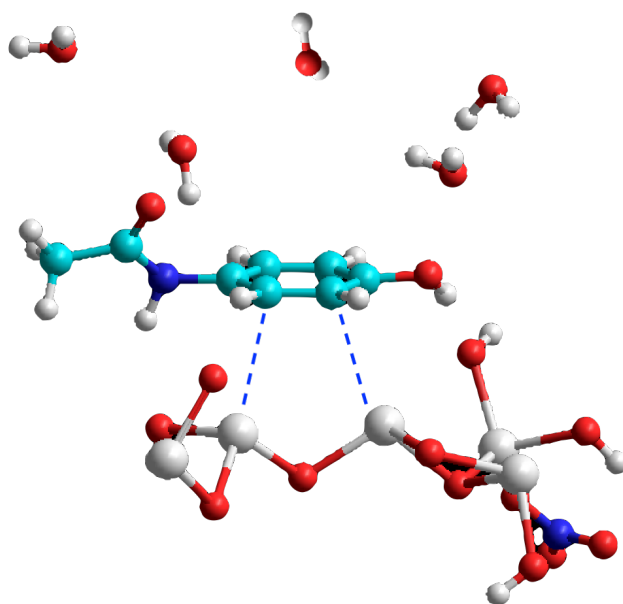


Figure 4.1 – Paracetamol and $\text{Bi}_5\text{O}_7\text{NO}_3$ cluster optimized geometry

by resistors in parallel: the one with the lowest resistance will see the most current pass through it. Hence, given the uncertainty of the computed values (plus the uncertainty associated with the Marcus Theory calculation) and the fact that the closest alternative configuration had inter-center distances much higher than the one in **Figure 4.1** it is reasonable to assume that the kinetic behavior of the system is best modeled by the chosen configuration. The difference in the (fictitious) bond lengths of some of the obtained interactions are summarized in **Table 4.1**. It should be noted that the rate constant that can be calculated macroscopically for a given electrochemical process will usually not be the same to the one predicted using just a computational model. In fact mass transport effects should be taken into account and also the possibility of chemical reactions changing the active species.

Configuration	Bond lengths	
B3-B4	3.8 Å	3.2 Å
B1-B2	5.4 Å	3.8 Å
B2-B3	5.8 Å	4.7 Å
B4-B5	6.3 Å	5.3 Å

Table 4.1 – Fictitious bond lengths of the different computed configurations

Here a rough intuitive model of the interplay of different phenomena leading to the actual Red/Ox reaction could be described by resistors in series, where the slowest step (resistor) will be the rate determining one. Regarding the geometrical arrangement of the system shown in **Figure 4.1**, a few additional considerations could be done:

- The approach of the paracetamol molecule towards the cluster can reach a stable state only if positioned in an roughly symmetrical position with regards to the cluster itself. This would suggest that the hydrogen bonds introduced to saturate the otherwise undercoordinated atoms makes the system unstable when the analyte molecule gets closer to them. Clearly the use of plane waves and periodic cells would probably give more accurate results, but for nanostructured materials with high surface area and a defective structure it may still be a reasonable approximation.
- An important steric effect is induced in the vicinity of the NO_3^- group, where the electronic density in the vicinity of the highly electronegative nitrogen atom tends to repel the π electron density of the aromatic ring of the paracetamol molecule.
- The presence of an amide group on the paracetamol molecule polarizes it and makes it so that a lower energy state is reached when it's oriented on the opposite side of NO_3^- group

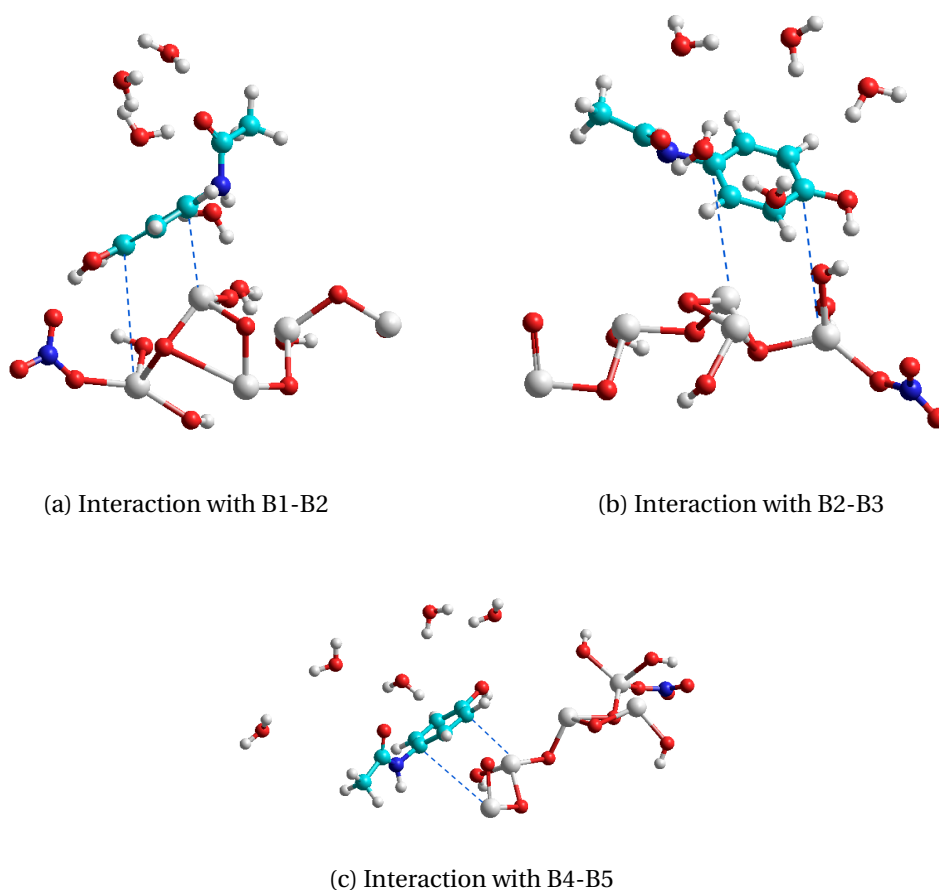


Figure 4.2 – Examples of alternative optimizations for different interactions geometries

Distribution of charge density To gain further information regarding the system under study, a 2D plot of the charge density was produced with HyperChem[®]. A 3D map was also possible to generate, however the graphical representation of the program is of difficult interpretation, hence it was decided not to use it. Accordingly, to obtain the plots in **Figure 4.3** and **4.4** two planes were chosen, such that they would be perpendicular to each other and passing through the π electronic density of the aromatic ring of paracetamol. Moreover, the first plane was also chosen so that it would highlight the charge density around the two bismuth atoms closest to the paracetamol molecule.

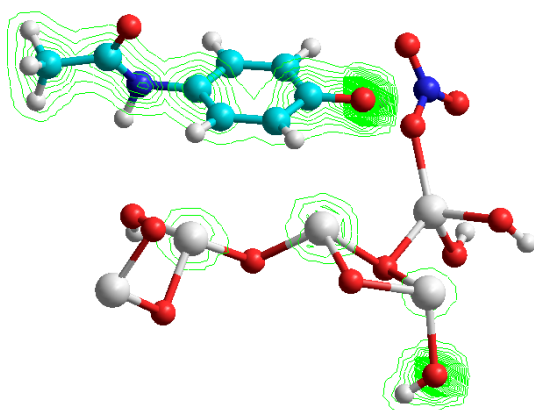


Figure 4.3 – Charge density for a plane passing through the aromatic ring of PCM and through the interacting Bi atoms of the cluster

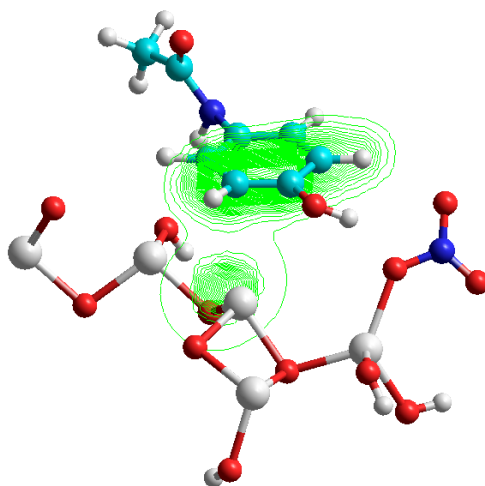


Figure 4.4 – Charge density for a plane passing through the aromatic ring of paracetamol and perpendicular to the axis of the two Bi atoms of the cluster interacting with PCM

Relevant molecular orbitals To add to the other results presented, the mapping of relevant molecular orbitals can give a better picture of the electron transfer process itself. In particular

the HOMO and the LUMO are shown in **Figure 4.5** and **4.6**, where it was decided for simplicity to not plot the orbital itself but Ψ^2 which is better related to the intuitive concept of probability of finding an electron (see the interpretation of the wavefunction formulated by Born in 1926).

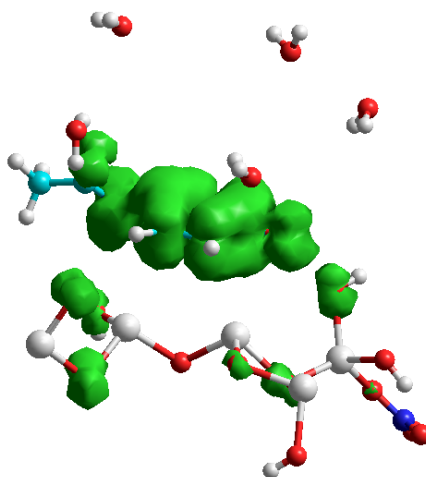


Figure 4.5 – HOMO of the system PCM- $\text{Bi}_5\text{O}_7\text{NO}_3$ cluster

Concerning the molecular orbitals plotted in **Figure 4.5** and **4.6** it is of particular interest their location, which tends to be limited either on the paracetamol or the bismuth subnitrate cluster. In fact the HOMO is almost exclusively localized on the aromatic ring of PCM, and the LUMO on the cluster. Since the configuration of the optimized system should at least on a theoretical basis give a possible transition state, this would suggest that in condition of (quasi) equilibrium the PCM molecule would be rich in filled states and easier to oxidize, and the cluster rich in unfilled states, thus easier to reduce.

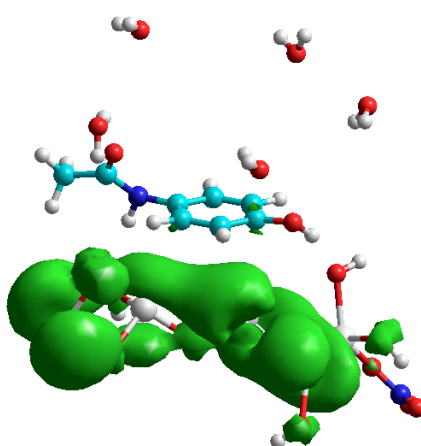


Figure 4.6 – LUMO of the system PCM- $\text{Bi}_5\text{O}_7\text{NO}_3$ cluster

4.1.1 Calculated rate constant and activation energy

For the selected configuration (B3-B4) which had reached a stable convergence in the calculated potential energy, the relevant energetic parameters were inserted in the generalized form of Marcus theory to obtain the energy of activation and the rate constant.

Configuration	Rate constant (ms ⁻¹)	Activation energy (eV)
B3-B4	3.2	9.8

Table 4.2 – Rate constant and activation energy of the optimized structure

A detailed description of the Marcus theory and its assumptions has been presented in **Section 2.1.3**. The transfer integral was calculated with the generalized Mulliken Hush theory (**Eq 2.9**). The rate constant is calculated from **Eq 2.8**, and the activation energy has its usual meaning in the context of Arrhenius theory and is defined by Marcus by:

$$E^* = \frac{(\Delta E + \lambda)^2}{4\lambda} \quad (4.1)$$

Where λ is the reorganization energy and ΔE is defined as

$$\Delta E = (-IP + EA + \Delta G_s^e + e^2/R) \quad (4.2)$$

The symbols of **Eq. 4.2** have same meaning as in **Section 2.1.3**.

The results agree well with the rate constant obtained experimentally from the cyclic voltammograms of SPEs functionalized with Bi₅O₇NO₃ (See **Table 4.4**). It should be noted that the calculated values slightly overestimate the experimental ones. This could be due to the fact that the computational calculation does not take into account the kinetic limitation of diffusion, thus de facto assuming the process as reversible. As described in detail in **Section 4.2.1** unfortunately the electrochemical process is quasi reversible. Thus the rate constants for the electron transfer and for diffusion are in the same range. Moreover the presence of reaction products could shield active sites of Bi₅O₇NO₃ and the carbon electrode reducing the measured rate constant. Finally there's an intrinsic uncertainty in the estimation of the k in both methods, be it computational or experimental. The limitations of the computational model have already been extensively highlighted. The application of the Laviron equation from cyclic voltammograms is in fact not an exact measurement but a good estimation based essentially on two parameters correlated with k. That is the coefficient of electron transfer (α) and the peak-to-peak separation (ΔE_p).

4.2 Cyclic Voltammetry

Cyclic Voltammetry has been performed to evaluate the electrocatalytic performance of the synthesized materials. The produced bismuth oxide and bismuth subnitrate heterostructures were deposited on the WE surface of commercial SPE (Dropsens DRP 110). As clarified in detail in **Section 3.1.2** a solution of 1mM of PCM was produced, and a CV experiment performed. The potential was cycled from -0.3V to 0.9V with with 6 different scan rates: 50mV, 100mV, 150mV, 200mV, 250mV, 300mV. With the aim of building an understanding of the underlying mechanisms governing the actual shape of the voltammograms, a brief introduction to the electrochemical response of the system is presented.

4.2.1 Electrochemical oxidation of Paracetamol in aqueous solutions

Figure 4.7 shows an example of a cyclic voltammogram of 1mM of paracetamol in 0.1M of PBS at pH 7.4 for a SPE. In the forward scan an anodic peak can be seen and it can be related to a 2 electron and 2 proton electrochemical reaction associated to the transformation of the paracetamol molecule to NAPQI as reported by Kissinger *et al.* [70]. This reaction presents a quasi-reversible character, meaning that the rate constant of electron transfer is similar to the rate constant of mass transfer.

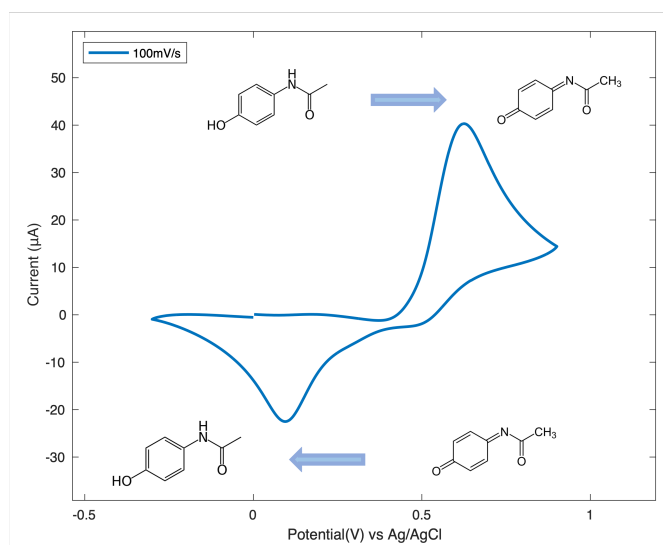


Figure 4.7 – Cyclic voltammogram of 1mM of paracetamol in 0.1M of PBS at pH 7.4 on a SPE

Given that there is also the participation of two protons in the electrochemical reaction, depending on the pH of the electrolytic solution different voltammograms will be obtained. The ratio of the cathodic and anodic peak currents I_{pc}/I_{pa} could be considered as a indication of the stability of the NAPQI, as indicated by **Figure 4.8**. For acidic (less than pH 4) and basic (more than 9) media it has been shown that the intensity of the cathodic peak is reduced, thus meaning a more stable NAPQI. Notably, at low pH NAPQI tends to hydrolyze, at high pH to

hydroxylate and at intermediate pH to dimerize.

In particular the electrochemical behavior of paracetamol in acidic media, and the almost nihil cathodic current, has been ascribed to the fast transformation into an intermediate which slowly converts to p-benzoquinone [29]. Conversely, in alkaline pH the Michael addition of an OH^- ion is favoured, so that the anodic reaction leads to the formation of not only NAPQI but also N-(2,4,5-trihydroxyphenyl)acetamide and p-benzoquinone.

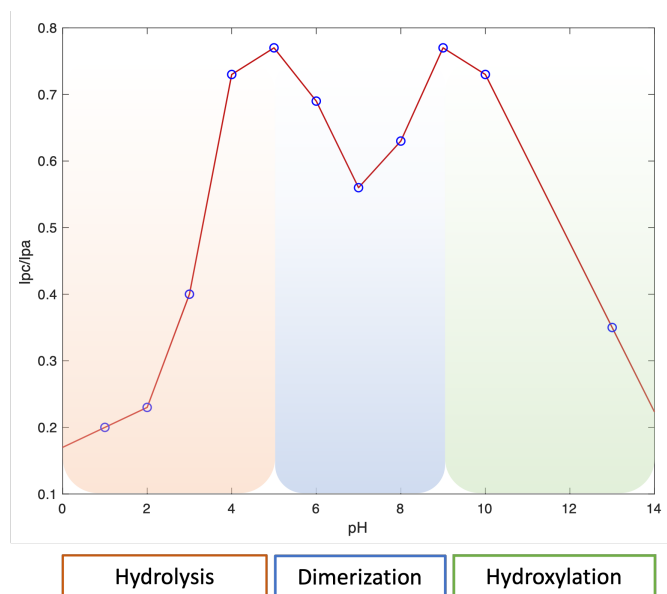


Figure 4.8 – Cathodic and anodic current peak ratio as a function of pH for paracetamol, as reported by Nematollahi *et al.* [29]

4.2.2 Preliminary electrochemical evaluations of the system

As an initial step of the study of the electrodes' behavior, it is important to highlight, through a direct comparison, the electrochemical response of the bare electrodes to a solution of 0.1M PBS and to a 0.1M PBS + 1mM PCM.

As shown in **Figure 4.9a** a clear difference can be discerned. In fact when the electrolytic solution is without the paracetamol molecule a mostly capacitive response is detected, where the non-faradaic currents are orders of magnitude smaller than with paracetamol molecule present. Moreover, as detailed in **Section 4.2.1** the electrochemical process of oxidation and subsequent reduction of the PCM molecule can be described as quasi-reversible. Such a characterization will be more clear when multiple voltammograms at different scan rates are considered. Anyhow the ratio between the anodic and the cathodic current is between 0.5 and 0.6 which is in very good agreement with previous studies of Nematollahi *et al.* [29].

It's been shown that the electrochemical response of the system is pH sensitive and that (approximately) between pH 6 and 8 NAPQI tends to dimerize, thus explaining the reduced

intensity of the cathodic peak. An further indication of the stability of the produced dimers

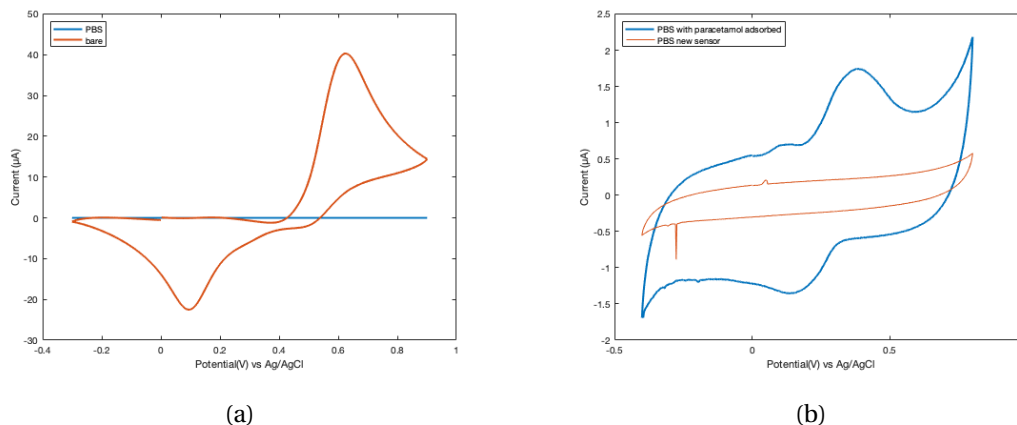


Figure 4.9 – (a) With and without PCM for a bare electrode, (b) Adsorption of PCM on a bare electrode after cleaning with DI water three times

was provided by evaluating if these species would readily adsorb on the WE or not. This was achieved by comparing the cyclic voltammogram of a never used bare electrode in PBS and a bare electrode subjected to 3 cycles of CV at 100mV/s and then cleaned 3 times with distilled water. In **Figure 4.9b** the result of this initial test is presented . A clear increase in the capacitive response can be seen, and possibly an Electrochemical Impedance Spectroscopy (EIS) study could further illuminate how the electrical double layer of the WE changes as a result of adsorption. Anyhow, even more importantly the cathodic and anodic peaks can be clearly discerned superimposed to the non-faradaic component.

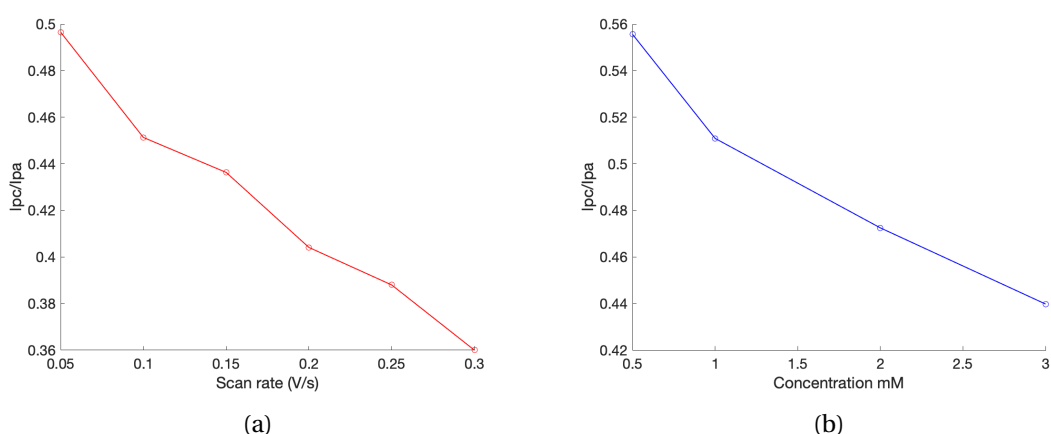


Figure 4.10 – (a) Current peak ratio as a function of scan rate for a bare electrode at a PCM concentration of 1mM, (b) Current peak ratio as a function of PCM concentration for a bare electrode

Looking at **Figure 4.10b** it can be seen that the ratio of the cathodic and anodic current peaks is dependent on the concentration of PCM. Thus a second order kinetic process is likely to happen, where the dimerization of NAPQI is subsequent to the electrochemical electron transfer. Moreover this is also reflected in **Figure 4.10a**, showing an inverse dependence on scan rate. This can be attributed to the formation of a thin film of dimers which makes the reduction of NAPQI more difficult. As an additional confirmation of the progressive (but mild) fouling of the WE surface it

4.2.3 Detailed characterization and kinetic study

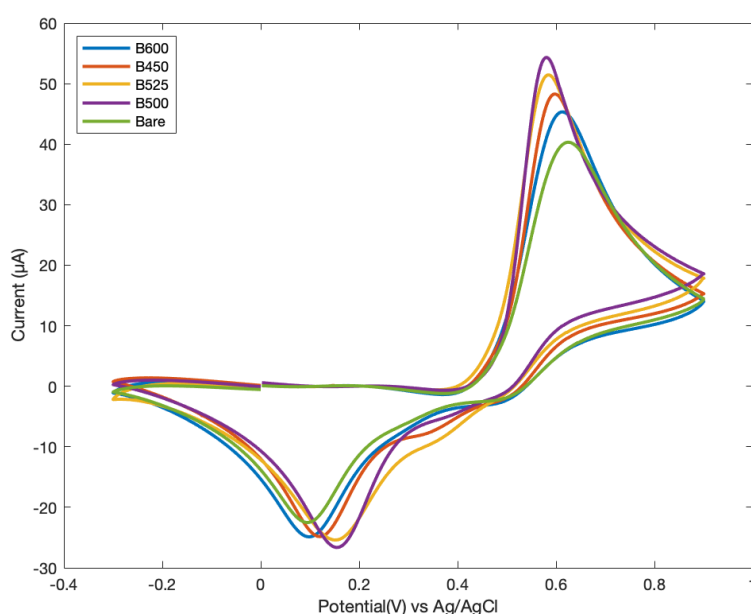


Figure 4.11 – Comprehensive overview of the voltammograms for the differently functionalized SPEs at a scan rate of 100mV/s in PBS at pH 7.4 and PCM concentration of 1mM

Material	Peak (μA)
Bare electrode	40.17 ± 0.51
B450	49.10 ± 1.2
B500	52.73 ± 1.0
B525	51.13 ± 0.92
B600	45.33 ± 0.69

Table 4.3 – Anodic peak currents for the different functionalized materials

In **Figure 4.11** the voltammograms of the functionalized SPE are presented. The electrolytic solution was 0.1M PBS at pH 7.4 and 1mM of PCM, and the scan rate 100mV/s. It can be seen that compared to the bare electrode an increase in the peak current is produced for all depositions. In fact, such a response can be attributed to the improved kinetics of electron

transfer between the analyte (PCM) and the WE due to the electrocatalytic effect of the bismuth oxide/subnitrate materials. In general the B500 and B525 perform better than the B450 and B600 leading to a possible hypothesis that the presence of different domains making up an heterostructure improves the catalytic activity. Previous work has shown that this is true for photocatalysis [45], due to the particular alignment of the electronic bands which causes an easier separation of electrons and holes. However for electrocatalysis what is actually relevant is the adsorption energy of the reactant and the desorption energy of the product. The main common point of photocatalysts and electrocatalyst is surely the surface area: in both cases the more area is exposed the better the performance. For this reason it is postulated that the difference between the different functionalization can be possibly attributed to morphological reasons. Though as of now, further studies should be conducted, such as X-ray Photoelectron Spectroscopy (XPS) and/or X-ray Diffraction Analysis (XRD) to be completely sure of the chemical and crystalline composition of the synthesized materials.

Material	k (ms ⁻¹)	D(cm ² /s)	ΔE _p (mV)	Alpha (α)
Bare electrode	0.49 ± 0.08	1.73 · 10 ⁻⁶	505 ± 5	0.488 ± 0.06
B450	1.51 ± 0.12	2.24 · 10 ⁻⁶	427 ± 10	0.441 ± 0.09
B500	1.84 ± 0.10	2.01 · 10 ⁻⁶	416 ± 10	0.418 ± 0.08
B525	1.77 ± 0.09	1.92 · 10 ⁻⁶	421 ± 7	0.422 ± 0.06
B600	0.98 ± 0.05	1.89 · 10 ⁻⁶	447 ± 6	0.453 ± 0.09

Table 4.4 – Energetic and kinetic parameters for the different materials, where k and D are calculated at a scan rate of 100 mV/s

Table 4.4 summarizes the relevant kinetic parameters obtained for three electrodes per type, with their respective means and standard errors. ΔE_p stands for the peak-to-peak separation (in mV) and can be taken as a measure of how favourable the electron transfer process actually is, similarly to the commonly used overpotential. For all electrodes ΔE_p is higher than 59mV/n where n=2, the number of electrons involved in the reaction. This inequality is a common diagnostic criteria for electrochemical reversibility, hence allowing to characterize the RedOx reaction of PCM on these SPE as quasi-reversible. The charge transfer coefficient (α) is instead an indication of how symmetric is the thermodynamic energy barrier for the oxidation and reduction processes. It was calculated by taking the slope of the regression line of the anodic and cathodic peaks positions with respect to the logarithm of the scan rate and then by considering the following relationship:

$$m_c \cdot RT \cdot \alpha nF = m_a \cdot RT \cdot (1 - \alpha) nF$$

After simplifying the equation:

$$\alpha = \frac{m_a}{m_c + m_a}$$

Where m_c and m_a are the slopes of the anodic and cathodic peak regression lines, and n=2 is the number of electron exchanged, as reported by multiple studies [70] [29]. The diffusion

coefficient D instead is calculated through the use of Randles-Ševčík equation at 100mV/s of scan rate, where after rearranging the following equation is obtained:

$$D = \left(\frac{i_p}{(0.446 \cdot n \cdot F \cdot A \cdot C)} \right)^2 \cdot (R \cdot T) / (n \cdot F \cdot v)$$

Where $A=0.12\text{cm}^2$ is the area of the WE surface, $n=2$ and the other symbols have the same meaning as in **Equation 2.21**. It's important to remark that the concentration of the oxidized species must be expressed in mol/cm^3 , and since for this calculation the voltammograms were obtained with a PCM of 1mM, the used value for the calculation was $10^{-6} \text{mol}/\text{cm}^3$. For the calculation at 100mV/s of the rate constant of electron transfer the Laviron equation is employed. Given that the condition of applicability $n\Delta E_p > 200\text{mV}$ is satisfied, the value of k can be calculated as follows:

$$\log(k) = \alpha \cdot \log(1 - \alpha) + (1 - \alpha) \cdot \log(\alpha) - \log(R \cdot T / (nFv)) - \alpha \cdot (1 - \alpha) \cdot n \cdot F \cdot \Delta E_p / (2.3 \cdot RT)$$

In **Figure 4.12a** multiple voltammograms performed on a bare electrode are presented. The scan rate is varied from 50 mV to 300 mV in steps of 50 mV and performed on a volume of 100 of 0.1M PBS + 1mM PCM dropped on the surface of the WE through the use of a pipette. The first thing that should be noted is the linear increase of the peak currents (anodic and cathodic) with respect to the square root of the scan rate. Thus following with good agreement Randles-Ševčík, indicating the that the system involves freely diffusing RedOx species. A linear

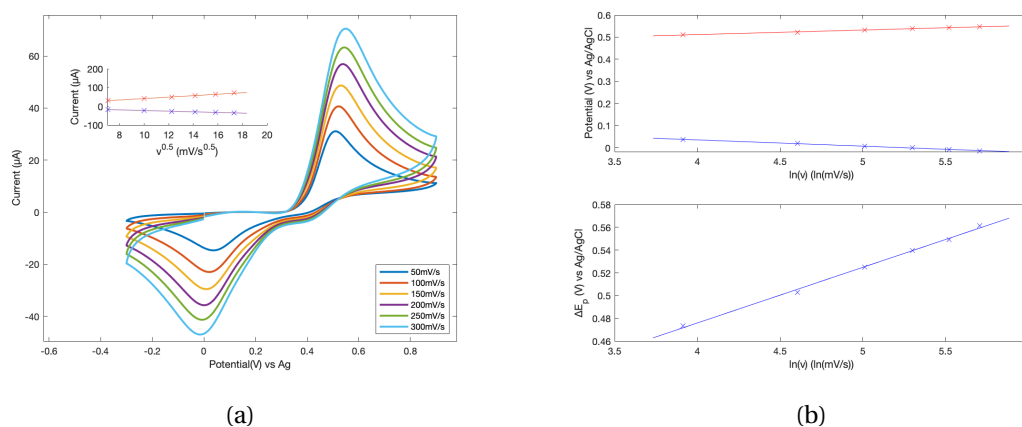


Figure 4.12 – (a) Cyclic voltammograms at different scan rates (from 50mV/s to 300mV/s in steps of 50mV/s) for a solution of 0.1M PBS with 1mM of PCM for a bare SPE, with the linear dependence of the peak currents on the square root of the scan rate, (b) plots showing the linear relationship of ΔE_p and E_{pa} , E_{pc} from $\ln(v)$

dependence on the scan rate would indicate instead substantial adsorption of the analyte on the WE surface. Though in **Figure 4.9b** it is shown that a measure of adsorption does happen, it appears not to affect in a drastic way the response of the sensor. Clearly this is true at least for the total number of cycles per experiment, that is $3 \times 6 = 18$, and further evaluations should be performed to see if fouling does happen.

Material	$I_{pa}(\mu A)$	R^2	$I_{pc}(\mu A)$	R^2
Bare electrode	$3.84 \sqrt{v} + 2.815$	0.996	$-1.743 \sqrt{v} - 5.318$	0.999
B450	$4.37 \sqrt{v} + 5.585$	0.992	$-1.986 \sqrt{v} - 7.400$	0.994
B500	$5.124 \sqrt{v} + 2.789$	0.995	$-3.281 \sqrt{v} - 1.741$	0.999
B525	$4.925 \sqrt{v} + 2.8520$	0.996	$-2.894 \sqrt{v} - 3.594$	0.999
B600	$4.295 \sqrt{v} + 2.432$	0.995	$-1.942 \sqrt{v} - 5.045$	0.998

Table 4.5 – Fitting parameter for anodic and cathodic peak currents with respective coefficient of determination

Moreover in **Figure 4.12b** the peak-to-peak separation and the peak positions are plotted against the natural logarithm of the scan rate. As the scan rate is increased the peak positions are shifted, leading to an increase in the peak to peak separation. Such a behavior is a further indication that the process is indeed quasi-reversible.

Table 4.6 summarizes the regression coefficients for ΔE_p with respect to $\ln(v)$.

Material	$\Delta E_p(\text{mV})$	R^2
Bare electrode	$48.87 \ln(v) + 280.50$	0.991
B450	$40.96 \ln(v) + 253.36$	0.993
B500	$49.89 \ln(v) + 185.07$	0.992
B525	$46.53 \ln(v) + 223.01$	0.988
B600	$47.88 \ln(v) + 235.770$	0.989

Table 4.6 – Linear regression equation for ΔE_p with respect to the logarithm of the scan rate

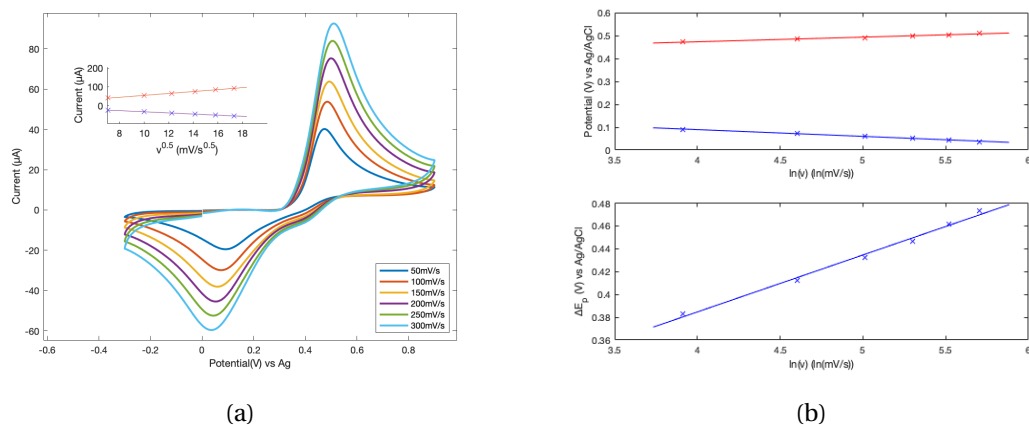


Figure 4.13 – (a) Cyclic voltammograms at different scan rates (from 50mV/s to 300mV/s in steps of 50mV/s) for a solution of 0.1M PBS with 1mM of PCM for a B500 functionalized SPE, with the linear dependence of the peak currents on the square root of the scan rate, (b) plots showing the linear relationship of ΔE_p and E_{pa} , E_{pc} from $\ln(v)$

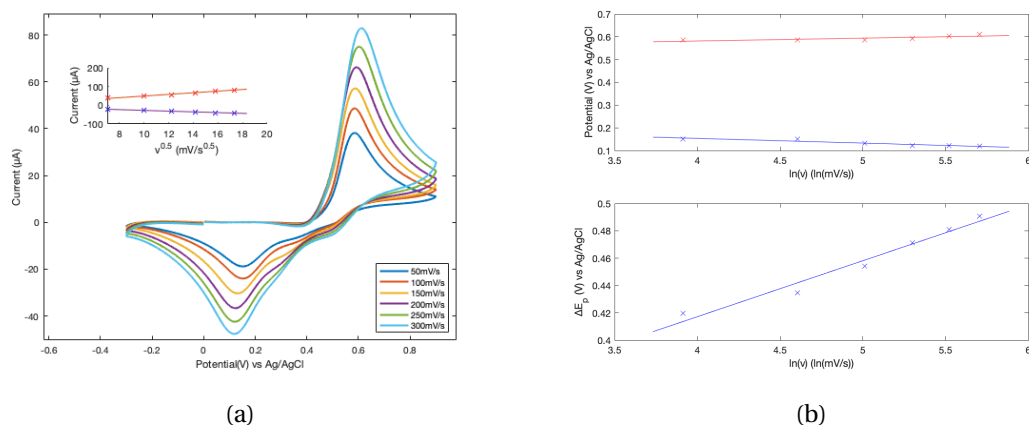


Figure 4.14 – (a) Cyclic voltammograms at different scan rates (from 50mV/s to 300mV/s in steps of 50mV/s) for a solution of 0.1M PBS with 1mM of PCM for a B450 functionalized SPE, with the linear dependence of the peak currents on the square root of the scan rate, (b) plots showing the linear relationship of ΔE_p and E_{pa} , E_{pc} from $\ln(v)$

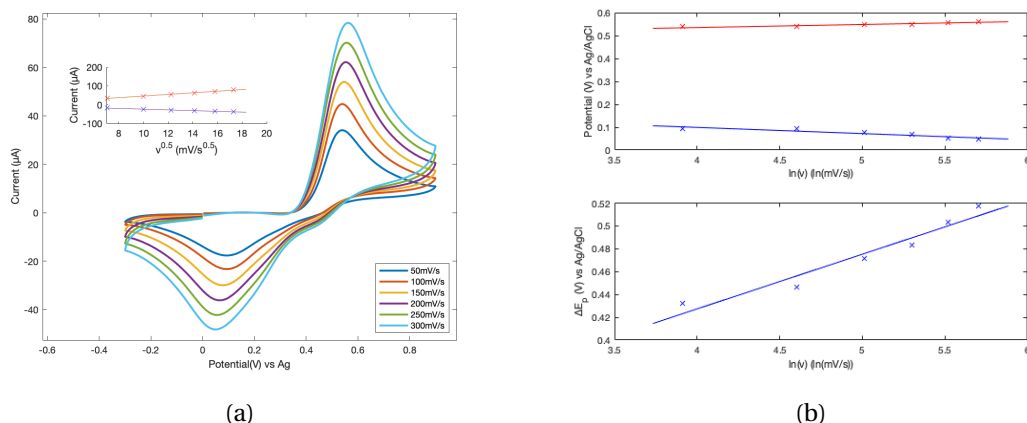


Figure 4.15 – (a) Cyclic voltammograms at different scan rates (from 50mV/s to 300mV/s in steps of 50mV/s) for a solution of 0.1M PBS with 1mM of PCM for a B600 functionalized SPE, with the linear dependence of the peak currents on the square root of the scan rate, (b) plots showing the linear relationship of ΔE_p and E_{pa} , E_{pc} from $\ln(v)$

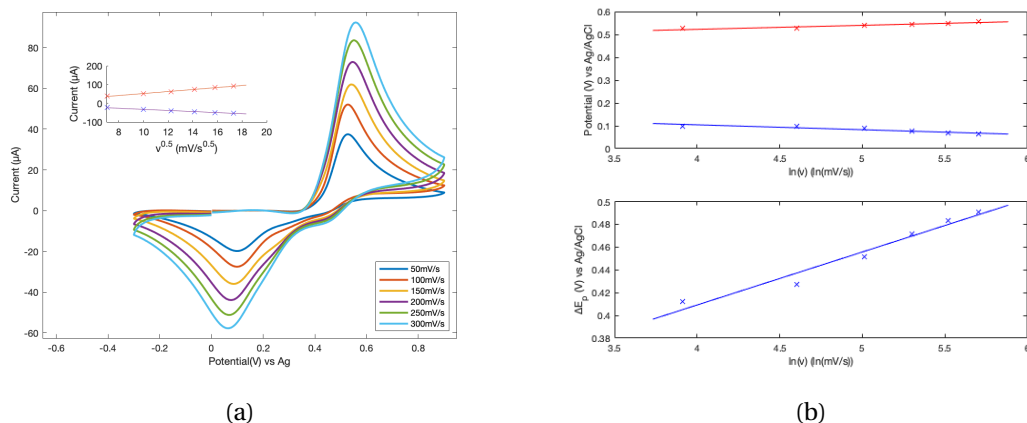


Figure 4.16 – (a) Cyclic voltammograms at different scan rates (from 50mV/s to 300mV/s in steps of 50mV/s) for a solution of 0.1M PBS with 1mM of PCM for a B525 functionalized SPE, with the linear dependence of the peak currents on the square root of the scan rate, (b) plots showing the linear relationship of ΔE_p and E_{pa} , E_{pc} from $\ln(v)$

4.2.4 Limit of detection and calibration curves

In order to characterize the performance of the different SPE it is important to evaluate their response at different analyte concentrations. CV at 100mV/s is thus performed at 4 different concentrations of PCM (0.5mM, 1mM, 2mM, 3mM) as described in **Section 3.5**. Then the peak anodic current is taken for each measurement (the third scan) and by plotting its value against the molar concentration a linear regression curve can be obtained. These measurement are performed for a total number of 3 sensors per type, so as to have sufficient statistical confidence in the reported values. Such a study is particularly important because it allows (within a certain limit of tolerance) to link the intensity of the sensor's response to a precise concentration, thus de facto making the sensor useful.

In **Figure 4.17** the different calibration curves are shown superimposed to one another to better highlight their differences and to allow the comparison between the slope of the bare and functionalized electrodes.

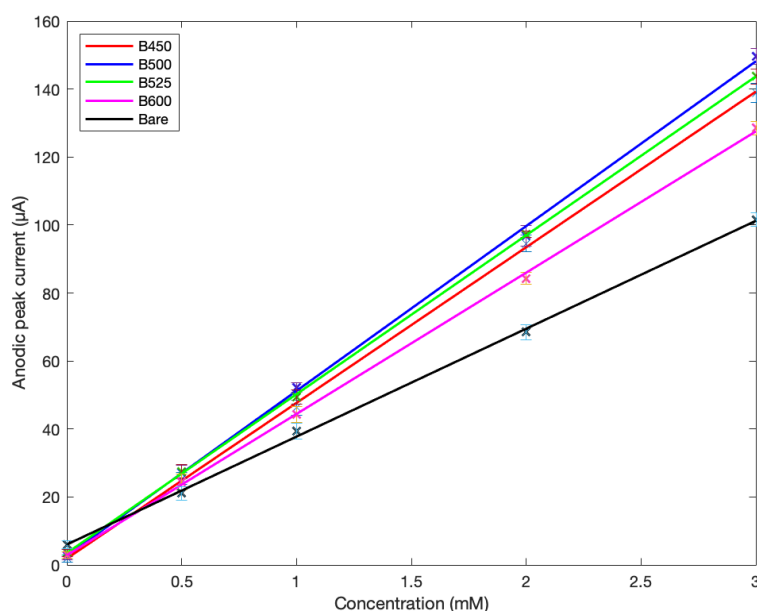


Figure 4.17 – Overview of the calibration curves for the differently functionalized SPEs at a scan rate of 100mV/s in PBS at pH 7.4 and PCM concentration of 0.5mM, 1mM, 2mM, 3mM

Material	Sensitivity ($\mu\text{A} / \text{mM}$)	LOD(μM)	RSD
Bare electrode	28.83 ± 0.15	3.642 ± 0.019	0.92%
B450	45.78 ± 0.33	4.484 ± 0.033	1.27%
B500	48.47 ± 0.32	4.208 ± 0.028	1.10%
B525	46.73 ± 0.38	4.391 ± 0.036	1.38%
B600	41.56 ± 0.25	4.714 ± 0.028	1.03%

Table 4.7 – Sensitivity and limit of detection for the different modified electrodes

From the slope of the curve the sensitivity was obtained, and the Standard Deviation (SD) for 3 samples calculated, which was then divided by the square root of the number of samples. Then by dividing the SD by the mean, the Relative Standard Deviation (RSD) was obtained. From the obtained result it can be clearly seen that the deposition of bismuth oxide / bismuth subnitrate species greatly improves the sensitivity of the sensor, almost doubling it. Moreover from this study a slight improved performance of the heterostructured B500 can be observed, and it's possible that this is due to a higher surface area due to the presence of nanochannels (See **Section 4.3**) or simply the presence of more favourable sites for adsorption, with low enough energy of desorption of the products of the electrochemical reaction.

Material	I_{pa}	R^2
Bare electrode	(28.83) C +6.25	0,999
B450	(45.78) C +1.89	0,999
B500	(48.47) C + 2.75	0,998
B525	(46.73) C + 3.51	0,999
B600	(41.56) C + 2.85	0,999

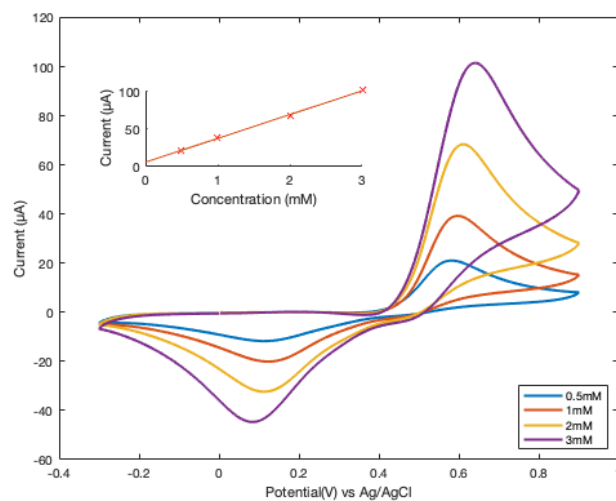
Table 4.8 – Fitting parameters for the calibration curves

The Limit of Detection (LOD) is minimum amount of a species that can be detected by a sensor from the blank measurement (in the absence of the analyte) within a certain confidence interval. To make the calculation and produce the results shown in **Table 4.7** the following formula was used:

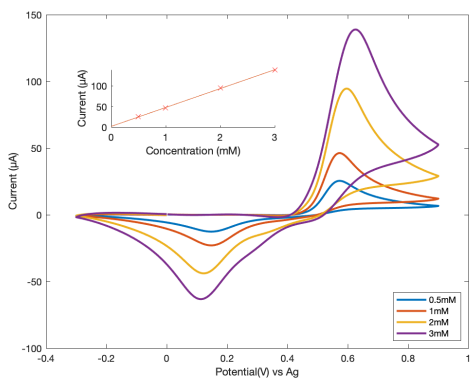
$$LOD = \frac{K * \sigma_x}{S}$$

Where σ_x is the standard deviation of the blank measurement, obtained by taking the intercept of the regression lines of the for each of the 3 sensors for each kind of sensor. K is a constant which depends on the desired confidence interval, 1 for 68.2%, 2 for 95.4%, 3 for 99.6 % (the one used in this study). Finally S is the calculated sensitivity. What can be observed is that the LOD is surprisingly lower for the bare electrode, even though the sensitivity, at the denominator, is smaller. At the same time however the standard deviation for the blank measurement for the functionalized sensors is higher, thus causing an modest increase in LOD nonetheless. The reason for this can be attributed to a series of factors:

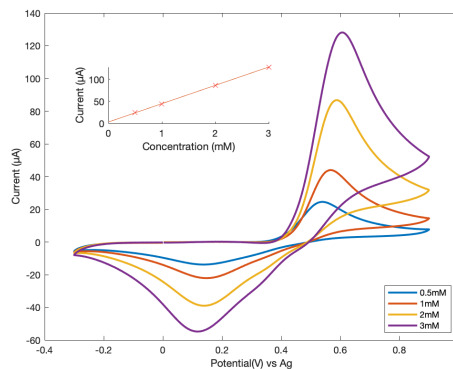
- The slope of the curve, i.e. the sensitivity, is increased, thus even for the same uncertainty on the angular coefficient the error on in intercept is evidently higher
- The process of drop casting is inherently imperfect in the deposition and coverage of particles, leading to a certain variability in the response of the sensors themselves



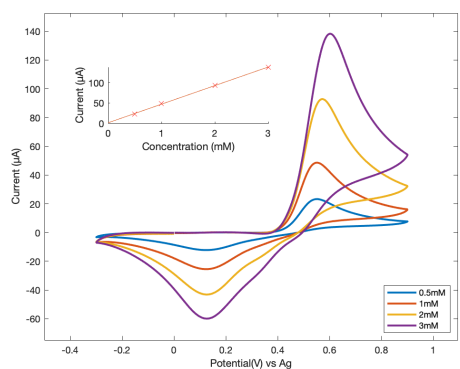
(a) Bare electrode calibration



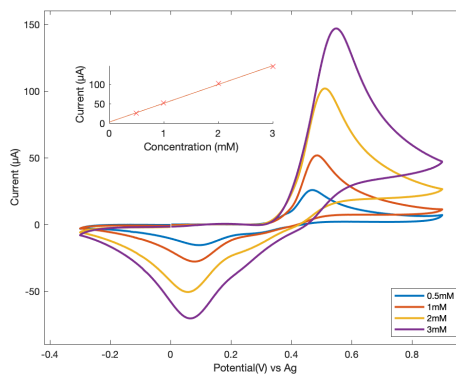
(b) B450 calibration



(c) B600 calibration



(d) B525 calibration

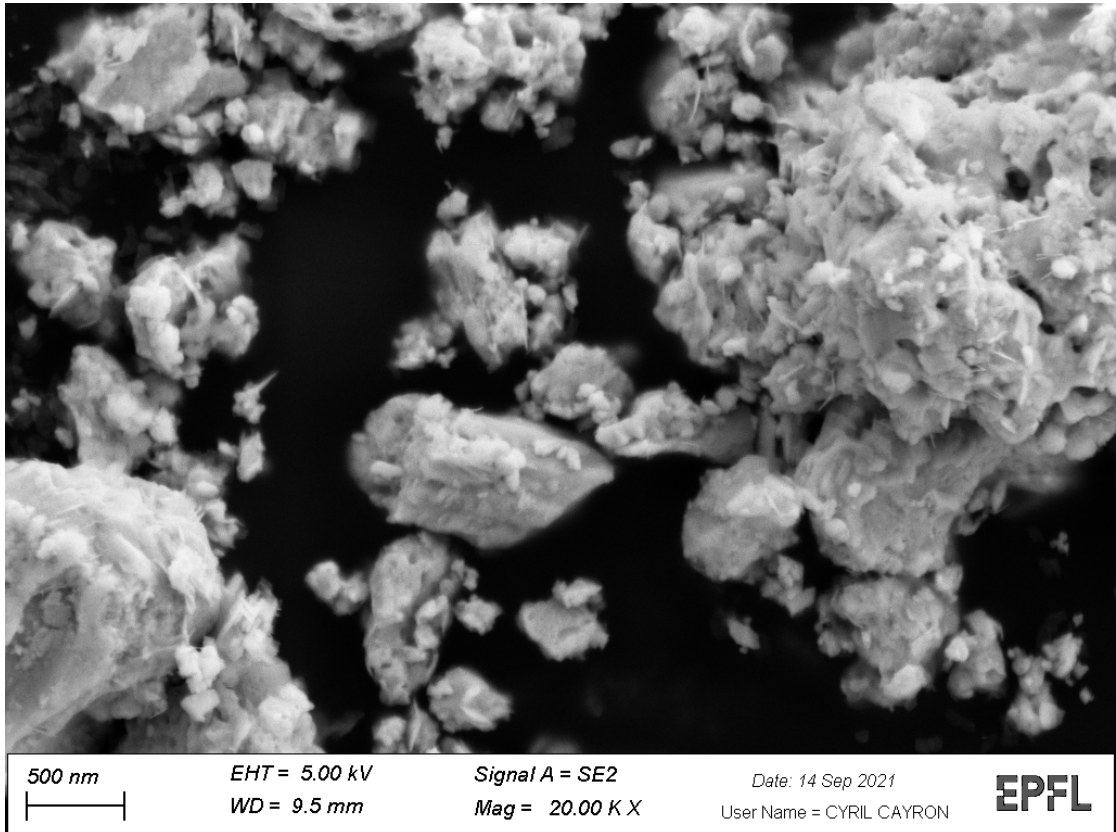


(e) B500 calibration

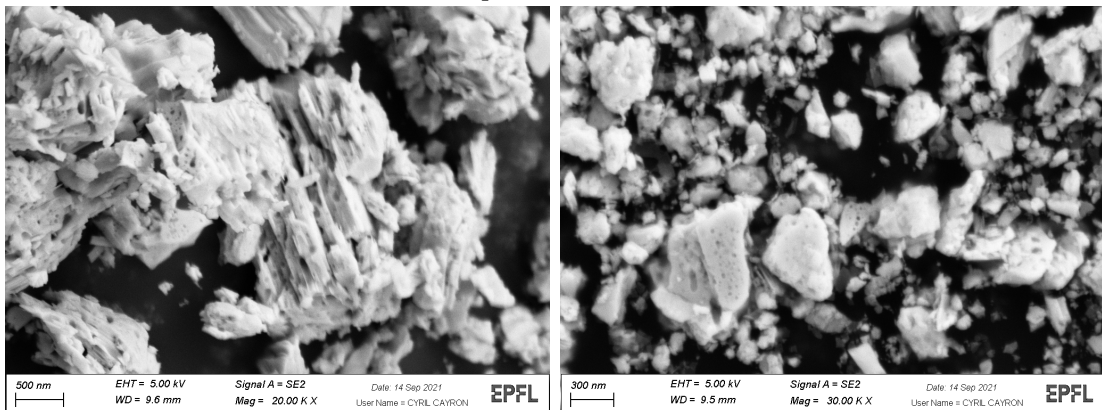
Figure 4.18 – Calibration curves for the different SPE studied, obtained at scan rate of 100mV/s and concentrations of PCM of 0.5mM, 1mM, 2mM,3mM in 0.1M PBS

4.3 Morphological characterization

To better inform the interpretation of the CV results, the synthesized powders were deposited on carbon tape and studied under the SEM, with a beam energy of 5KeV. The secondary electrons were acquired. A trend from an irregular particulate structure to progressively more lamellar can be seen, as the calcination temperature increases. This is in good agreement with the work of Gadhi *et al.* [45].



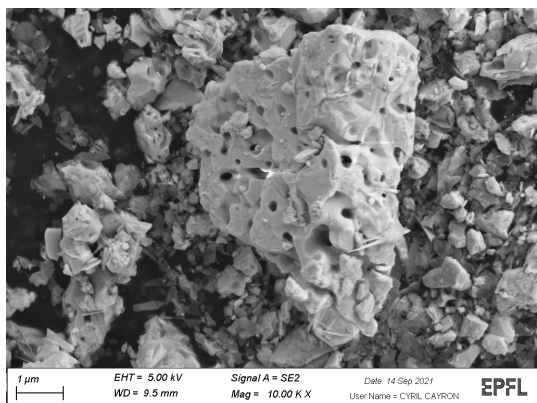
(a) B450 powder under the SEM



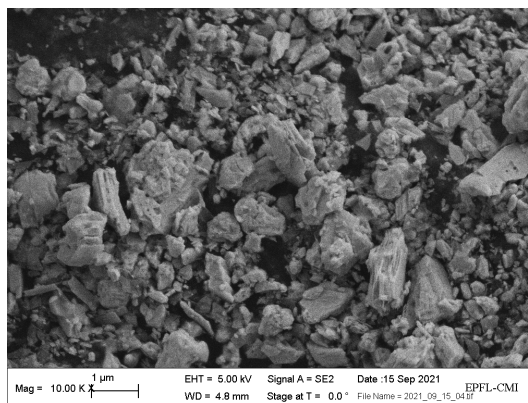
(b) B500 powder under the SEM

(c) B500 powder under the SEM

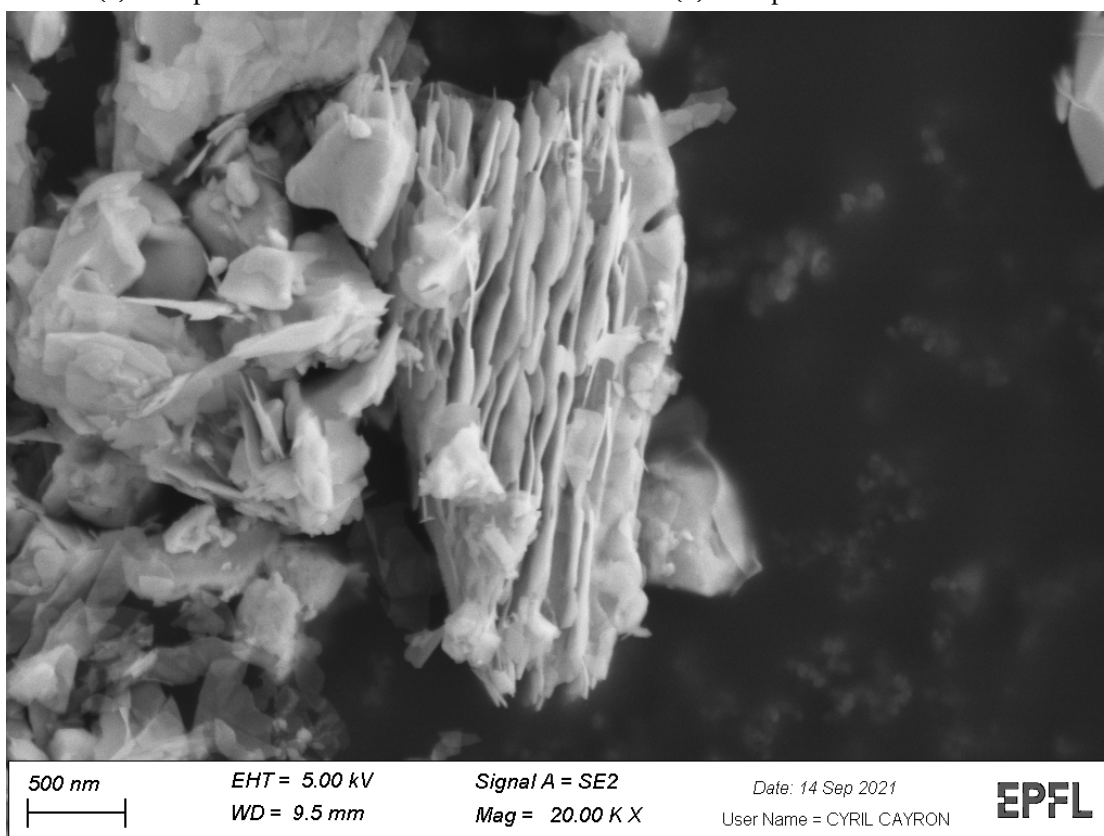
The structure of B450 appears composed of a series of micrometric aggregates with nanometric particles on its surface. Interestingly B500 is characterized by a series of nanochannels (possibly due to the expulsion of Nitric Oxide) which could be the reason for its better catalytic performance. The B525 still shows a (larger) porous structure, but with a slight lamellar nature. Finally for B550 the structure appears mainly lamellar.



(a) B525 powder under the SEM



(b) B525 powder under the SEM



(c) B550 powder under the SEM

4.4 Raman Spectra

Different Raman spectra are shown in **Figure 4.21** for $\text{Bi}(\text{NO}_3)_3 \cdot 5\text{H}_2\text{O}$ heated at different temperatures. In accordance with the work of Gadhi *et al* [78] the Raman spectra for the synthesized materials from 400C° to 450C° are essentially the same, since in this temperature range the $\text{Bi}_5\text{O}_7\text{NO}_3$ is stable. As a consequence, for simplicity they are not shown, so to better highlight the evolution from subnitrate to oxide. Moreover, 200 cm^{-1} were chosen as a starting point for the plot, since the data acquired at lower Raman shift was considered unreliable due to the Rayleigh component.

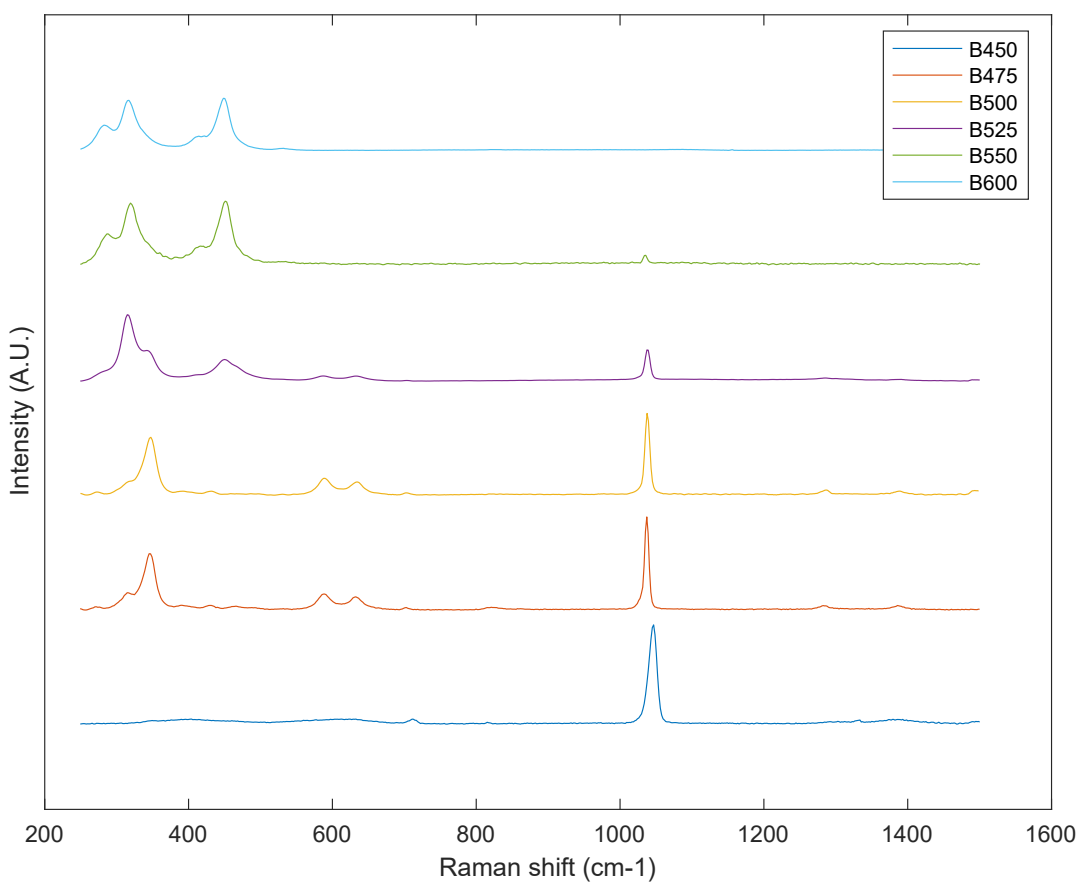


Figure 4.21 – Raman analysis of different materials obtained by solid state synthesis

Looking at the spectrum of the sample B450 it's possible to distinguish only one peak at 1049 cm^{-1} . Given that during the calcination of $\text{Bi}(\text{NO}_3)_3 \cdot 5\text{H}_2\text{O}$ starting from $\approx 400\text{ C}^\circ$ the following reaction occurs [80]:



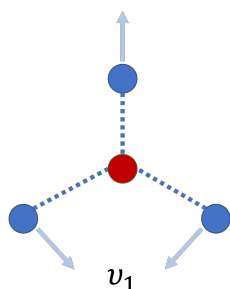


Figure 4.22 – Vibrational moment associated with the Raman peak at 1049 cm^{-1}

Because one of the products is nitric oxide, and since as the temperature increases the intensity of the peak at 1049 cm^{-1} diminishes, it was postulated that it could be relative to the NO_3^- group. This hypothesis finds confirmation in the work of [83] where the Raman spectra of different nitrates in aqueous solution were studied and an asymmetric peak at 1049 cm^{-1} was identified as related to the vibrational moment shown in **Figure 4.22**. Moreover an ulterior confirmation can be found in the book of Nakamoto [84], under the table relative to the vibrational frequency for XY_3 type planar molecules. Additionally it was noted that the main difference in the NO_3^- peak for solid nitrates or in solution is not in Raman shift but in the width of the peak itself. This can be explained by the additional degrees of freedom that the nitrate ions have in solution that results in a widened peak. Moreover it can be noted that as the temperature of calcination increases from 450 C° to 475 C° and the nitrate peak decreases in intensity, the peak shifts to lower Raman shifts ($\approx 5\text{ cm}^{-1}$), and after 475 C° it stabilizes. This particular phenomenon is very likely associated with a perturbation to the crystal structure of the sample due to the progressive transformation to bismuth oxide which in turn causes the nitrate ions to scatter at a lower frequency (with respect to the incident light). In fact from classical perturbation theory it is reasonable to assume that such a shift is related to an increase in the N-O bonds length, possibly due to the collapse of the column of nitrate groups described by Ziegler *et al* [77], which in turn causes stronger interaction with the surrounding lattice. A similar phenomenon was reported by Rossignol *et al* [85] with Zr-Pr mixed oxides, and by Kotula *et al* [86] with polycaprolactone.

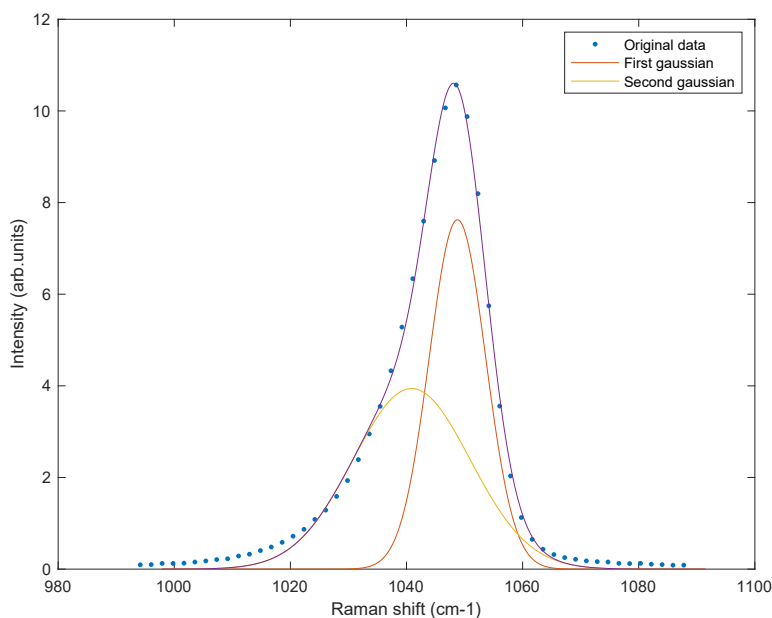


Figure 4.23 – Fitting of NO_3^- peak for B400

To accompany the above considerations with the use of MATLAB[®] the peak at 1049 cm^{-1} was fitted with two gaussians (**Figure 4.23**) allowing to underline its asymmetry. With regards to **Figure 4.21**, it's clear that as the calcination temperature increases, not only does the nitrate peak tend to vanish but also the emergence of multiple peaks at Raman shifts lower than 700 cm^{-1} can be noted as well. In particular, for the B475 and B500 samples two peaks at 585 cm^{-1} and 635 cm^{-1} respectively can be noted and were fitted with gaussian functions as well, as shown in **Figure 4.24**. Since at higher temperatures they tend to disappear it's probable that they are associated with intermediate phases, or the result of the interaction between the regions of Bi_2O_3 and $\text{Bi}_5\text{O}_7\text{NO}_3$.

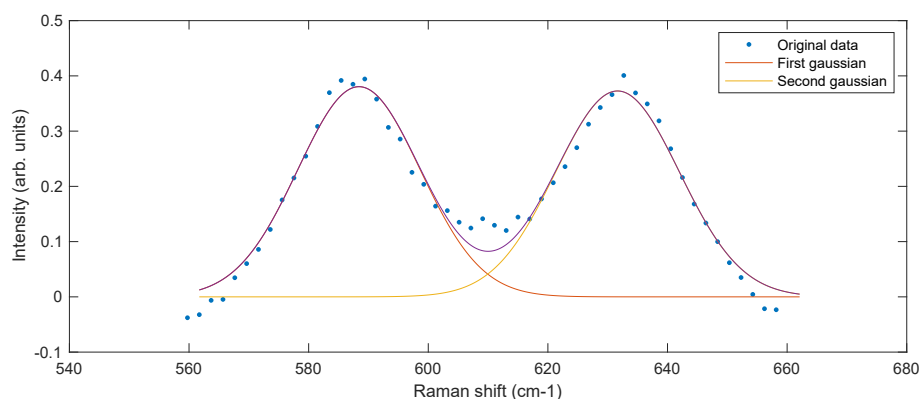


Figure 4.24 – Fitting of small peaks for B525

Interestingly another evolution in the Raman spectrum of the samples can be discerned: starting from a 475 C° until 600 C° a total of 5 peaks at a Raman shift less than 680 cm^{-1} start to emerge as the calcination temperature increases. From the work of [78] we know that a progressive transformation to bismuth oxide is to be expected. Hence, B600 sample could be intended as the natural limiting case where the bismuth (sub)nitrate is completely oxidized to Bi_2O_3 . To best fit the spectrum of the B600 sample, lorentzian functions were used.

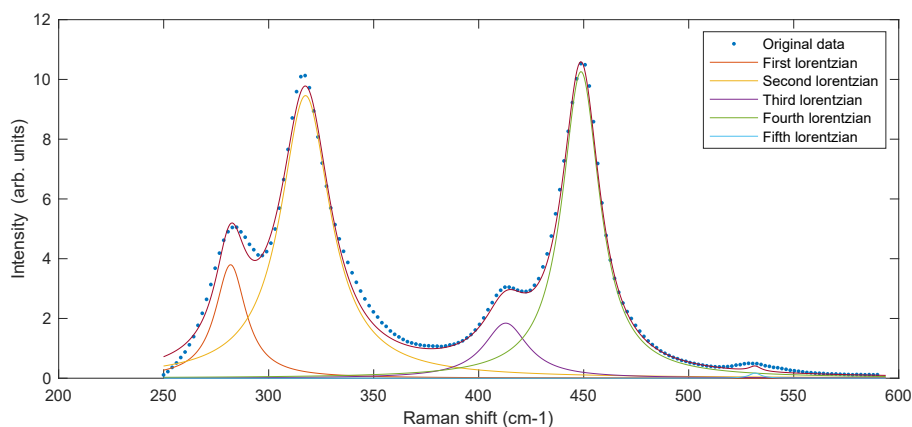


Figure 4.25 – Fitting of Bi_2O_3 peaks

5 Appendix

5.1 Preliminary test on a C-paper modified electrochemical cell

A tentative study using carbon paper as WE was performed. The electrolytic solution was 0.1M PBS and the concentration of PCM was 1mM. The scan rate was varied from 50mV/s to 300mV/s in steps of 50mV/s, so as to perform a kinetic study. In **Figure 5.1** an improvement in the peak current accompanied by a reduced peak-to-peak separation can be discerned for the functionalized carbon paper. It is postulated that the reason for the bad performance of the B600 functionalized electrode is due to its low solubility in ethyl alcohol, leading to a deposition of few and mostly micrometric aggregates. This study thus informed the main work on SPE where the materials were deposited in aqueous and not alcoholic dispersions.

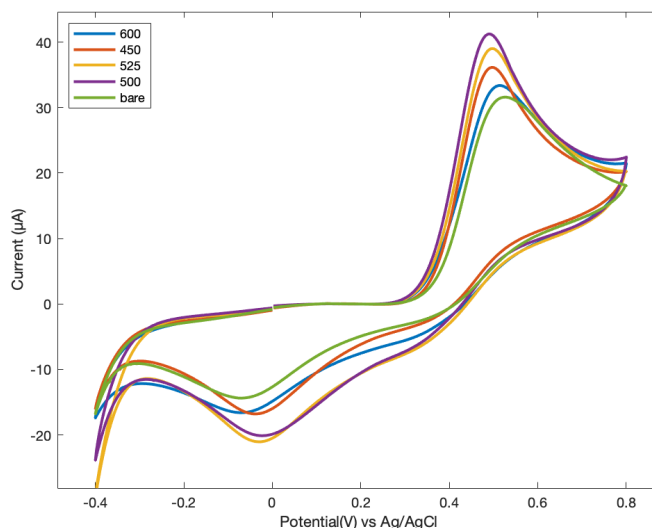


Figure 5.1 – Comprehensive overview of the voltammograms for the differently functionalized carbon paper electrodes at a scan rate of 100mV/s in PBS at pH 7.4 and PCM concentration of 1mM

Material	Peak (μA)
Bare electrode	$31.49 \pm 0,89$
B450	$36.13 \pm 1,34$
B500	$40.4 \pm 1,24$
B525	$39.5 \pm 1,13$
B600	$33.36 \pm 1,05$

Table 5.1 – Anodic peak currents for the different functionalized materials

In **Table 5.2** a summary of the relevant parameters are shown. The kinetic rate constants appear to be almost one order of magnitude smaller than the values calculated for the SPE of **Section 4.2.3**. Such a difference can be attributed to the increased electric resistance of the assembled electrochemical cell compared to a commercial SPE. In fact the conductive lines for the SPE are silver-based whereas in this cell the current would pass through electric crocodiles and then through the carbon paper itself. A possible solution to this problem could be to deposit silver paste on a portion of the carbon paper to produce a better conductive line and then isolating with epoxy resin near the portion that would be immersed (to avoid the electrochemical response of the Ag ions).

	Bare	450	500	525	600
$k(\text{ms}^{-1})$	$0,011 \pm 0.017$	$0,247 \pm 0.053$	$0,715 \pm 0.106$	$0,338 \pm 0.0744$	$0,301 \pm 0.067$
alfa (α)	$0,56 \pm 0.064$	$0,411 \pm 0.076$	$0,395 \pm 0.082$	$0,441 \pm 0.074$	$0,549 \pm 0.099$
$D (\text{cm}^2/\text{s})$	$1,07 \cdot 10^{-6}$	$1,87 \cdot 10^{-6}$	$3,43 \cdot 10^{-6}$	$2,68 \cdot 10^{-6}$	$1,43 \cdot 10^{-6}$
$\Delta E_p (\text{meV})$	620 ± 13	530 ± 18	510 ± 10	520 ± 7	590 ± 12

Table 5.2 – Summary of relevant parameters of a tentative study of carbon paper electrodes functionalized with the synthesized materials

Given that the peak current is linearly dependent on the WE surface area (see Randles-Ševčík equation) it was necessary to normalize the current with respect to the area A. Thus, through the use of an Hirox optical microscope the area of each fabricated electrode was measured. Then after the normalization, it was scaled so as to be relative to a 0.12 cm^2 area, the same as the SPE, so as to facilitate a comparison. Moreover the RSD was calculated for each set of electrodes so as to give an indication of the fabrication method precision.

	Bare	B450	B500	B525	B600
Mean (cm^2)	0,174	0,185	0,191	0,180	0,162
Std. (cm^2)	0,011	0,022	0,012	0,020	0,007
Relative Std.	6,12%	11,85%	6,09%	11,04%	4,29%

Table 5.3 – Carbon paper electrodes dimension variability expressed in terms of relative standard deviation

5.2 Paper based electrode proof-of-concept results

The add to the work done on carbon paper and the commercial SPE, a paper based electrochemical sensor was produced. The fabrication method has been described in detail in **Section 3.7**, and it's been designed so as not to require expensive laboratory equipment. Clearly this comes at the cost of reproducibility, but for a single proof-of-concept prototype it was considered satisfactory. In **Figure 5.2a** one of the first iterations of the produced sensors are presented, where the effect of the Ag ions from the silver paste is evident. The potential at which the PCM has its anodic peak is much higher than the Ag anodic peak. Hence it could be easily filtered after the acquisition.

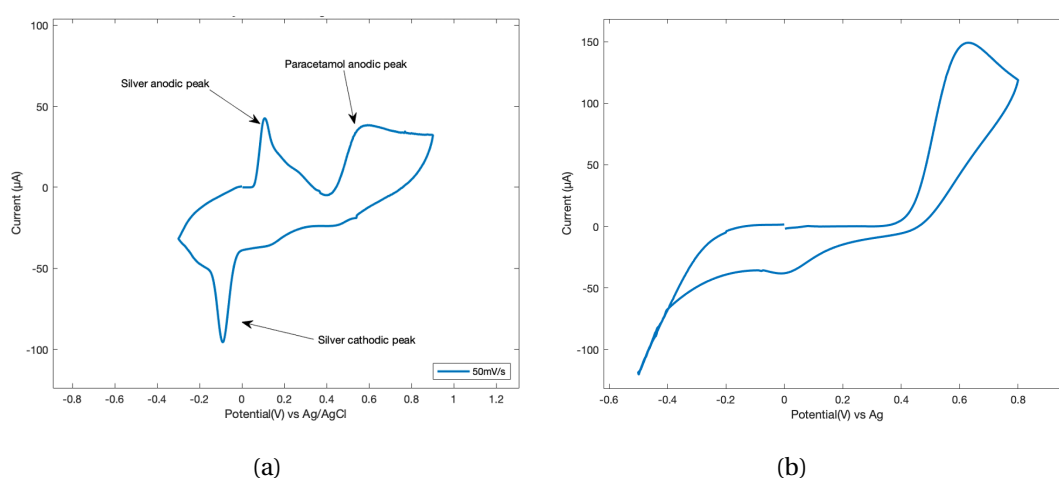


Figure 5.2 – (a) First iteration of a paper based electrode at a scan rate of 50mV/s in PBS at pH 7.4 and PCM concentration of 3mM (b) Second iteration of a paper based electrode at a scan rate of 150mV/s in PBS at pH 7.4 and PCM concentration of 3mM

However a clean voltammogram is desirable if a reasonable characterization is to be made. For this reason multiple iterations have been tried and finally it was observed that isolating the space between the electrodes with epoxy resin avoided the Ag ions interference. Moreover the electrical contact of the silver lines with the carbon paper was also changed from carbon paste to silver paste. A improved response was consequently seen as a result, as shown in **Figure 5.2b**.

6 Conclusions

The computational work done with a semi-empirical method allowed to evaluate the interaction of a molecule of PCM with a cluster of $\text{Bi}_5\text{O}_7\text{NO}_3$. In particular it was observed a steric repulsion between the NO_3^- ion of the cluster and the π electron density of the aromatic ring of PCM. Moreover, a symmetric approach of PCM was determined to be the only one leading to an a stable configuration, possibly due to the destabilizing effect of the hydrogen bonds introduced to saturate otherwise undercoordinated atoms at the border of the cluster itself. The amide group on PCM causes a polarization which in turn makes the system more stable if the molecule is oriented with the amide group opposite to the nitrate ion. For the optimized configuration of the system a rate constant of 3.2 ms^{-1} and an activation energy of 9.8 eV was obtained. This computational work set the basis for a theoretical framework aimed at evaluating the effect of the deliberate introduction of defects into the structure of a subnitrate species. In particular, through a solid state method heterostructures of $\text{Bi}_2\text{O}_3/\text{Bi}_5\text{O}_7\text{NO}_3$ were produced. The obtained materials were thus characterized via Raman Spectroscopy, where the peak at 1049 cm^{-1} was identified as relative to a vibrational moment of the nitrate ion. Consequently based on this analysis 4 samples (B450, B500, B525, B600) were chosen to be deposited on the working electrode of screen printed sensors (Dropsens DRP110). The performance of the sensors was evaluated via CV. The electrolytic solution was composed of 0.1M PBS and 1mM of PCM and the scan rate varied from 50mV/s to 300mV/s in steps of 50mV/s. The bare electrode showed a mean peak to peak separation of ΔE_p of 510 mV, whereas the best performing heterostructure 416 mV. Instead the allegedly single phase B450 presented a mean ΔE_p of 427 mV. The peak currents for all the functionalized sensors had an increase of around 30% where the best performing one was B500, and the worst B600. The calibration curves of the sensors were obtained by performing a CV for a 0.1M PBS at 0.5mM, 1mM, 2mM, 3mM of PCM. A linear response was observed, where the mean sensitivity of the bare electrode calculated at $28 \mu\text{A} / \text{mM}$ and a LOD of $3.64 \mu\text{M}$. The improvement in terms of sensitivity was observed to be approximately 70% for the functionalized materials, where still the best performance was seen in B500 and the worst in B600. Finally the fabricated paper-based sensor showed a very promising performance, comparable to a cell composed of C-paper as a WE, Ag/AgCl as a RE and Pt plate as a CE.

Bibliography

- [1] K. Cammann, "Bio-sensors based on ion-selective electrodes," *Fresenius' Zeitschrift für analytische Chemie*, vol. 287, no. 1, pp. 1–9, 1977, ISSN: 0016-1152. DOI: 10.1007/bf00539519.
- [2] S. P. J. Higson and P. M. Vadgama, "Biosensors: a viable monitoring technology?" *Medical and Biological Engineering and Computing*, vol. 32, no. 6, pp. 601–609, 1994, ISSN: 0140-0118. DOI: 10.1007/bf02524233.
- [3] W. C. Mak, *Malhotra, Banshi Dhar, Pandey, Chandra Mouli (Eds.), Biosensors: Fundamentals and Applications. Smithers Rapra Technology Ltd, ISBN: 978-1-91024-278-0, £85. Ser. Biosensors and Bioelectronics. 2018, vol. 104. DOI: 10.1016/j.bios.2017.12.026.*
- [4] S. Mohanty and E. Kougiyanos, "Biosensors: a tutorial review," *IEEE Potentials*, vol. 25, no. 2, pp. 35–40, 2006, ISSN: 0278-6648. DOI: 10.1109/mp.2006.1649009.
- [5] G. K. Mishra, A. Barfidokht, F. Tehrani, and R. K. Mishra, "Food safety analysis using electrochemical biosensors," *Foods*, vol. 7, no. 9, p. 141, 2018, ISSN: 2304-8158. DOI: 10.3390/foods7090141.
- [6] T. A. Saleh, G. Fadillah, and O. A. Saputra, "Nanoparticles as components of electrochemical sensing platforms for the detection of petroleum pollutants: a review," *TrAC Trends in Analytical Chemistry*, vol. 118, pp. 194–206, 2019, ISSN: 0165-9936. DOI: 10.1016/j.trac.2019.05.045.
- [7] M. Badihi-Mossberg, V. Buchner, and J. Rishpon, "Electrochemical biosensors for pollutants in the environment," *Electroanalysis*, vol. 19, no. 19-20, pp. 2015–2028, 2007, ISSN: 1521-4109. DOI: 10.1002/elan.200703946.
- [8] J. F. Rusling and R. J. Forster, "Biosensors designed for clinical applications," *Biomedicines*, vol. 9, no. 7, p. 702, 2021, ISSN: 2227-9059. DOI: 10.3390/biomedicines9070702.
- [9] R. Monošík, M. Stred'anský, and E. Šturdík, "Application of electrochemical biosensors in clinical diagnosis," *Journal of Clinical Laboratory Analysis*, vol. 26, no. 1, pp. 22–34, 2012, ISSN: 1098-2825. DOI: 10.1002/jcla.20500.
- [10] H. Teymourian, A. Barfidokht, and J. Wang, "Electrochemical glucose sensors in diabetes management: an updated review (2010–2020)," *Chemical Society Reviews*, vol. 49, no. 21, pp. 7671–7709, 2020, ISSN: 0306-0012. DOI: 10.1039/d0cs00304b.

- [11] D.-W. Hwang, S. Lee, M. Seo, and T. D. Chung, "Recent advances in electrochemical non-enzymatic glucose sensors – a review," *Analytica Chimica Acta*, vol. 1033, pp. 1–34, 2018, ISSN: 0003-2670. DOI: 10.1016/j.aca.2018.05.051.
- [12] V. K. Khanna, "Nanomaterials and their properties," in *Integrated Nanoelectronics: Nanoscale CMOS, Post-CMOS and Allied Nanotechnologies*. New Delhi: Springer India, 2016, pp. 25–41, ISBN: 978-81-322-3625-2. DOI: 10.1007/978-81-322-3625-2_3. [Online]. Available: https://doi.org/10.1007/978-81-322-3625-2_3.
- [13] N. R. Mohamad, N. H. C. Marzuki, N. A. Buang, F. Huyop, and R. A. Wahab, "An overview of technologies for immobilization of enzymes and surface analysis techniques for immobilized enzymes," *Biotechnology Biotechnological Equipment*, vol. 29, no. 2, pp. 205–220, 2015, ISSN: 1310-2818. DOI: 10.1080/13102818.2015.1008192.
- [14] D. Antuña-Jiménez, M. B. González-García, D. Hernández-Santos, and P. Fanjul-Bolado, "Screen-printed electrodes modified with metal nanoparticles for small molecule sensing," *Biosensors*, vol. 10, no. 2, p. 9, 2020. DOI: 10.3390/bios10020009.
- [15] M. Li, Y.-T. Li, D.-W. Li, and Y.-T. Long, "Recent developments and applications of screen-printed electrodes in environmental assays—a review," *Analytica Chimica Acta*, vol. 734, pp. 31–44, 2012, ISSN: 0003-2670. DOI: 10.1016/j.aca.2012.05.018.
- [16] F. Criscuolo, I. N. Hanitra, S. Aiassa, I. Taurino, N. Oliva, S. Carrara, and G. D. Micheli, "Wearable multifunctional sweat-sensing system for efficient healthcare monitoring," *Sensors and Actuators B: Chemical*, vol. 328, p. 129 017, 2021, ISSN: 0925-4005. DOI: 10.1016/j.snb.2020.129017.
- [17] H. GRAF, "Telemetry of plaque ph from interdental areas," *Helv. Odont. Acta*, vol. 10, pp. 94–101, 1966. [Online]. Available: <https://ci.nii.ac.jp/naid/10011007784/en/>.
- [18] S. Iguchi, H. Kudo, T. Saito, M. Ogawa, H. Saito, K. Otsuka, A. Funakubo, and K. Mitsubayashi, "A flexible and wearable biosensor for tear glucose measurement," *Biomedical Microdevices*, vol. 9, no. 4, pp. 603–609, 2007, ISSN: 1387-2176. DOI: 10.1007/s10544-007-9073-3.
- [19] H. C. Ates, J. A. Roberts, J. Lipman, A. E. Cass, G. A. Urban, and C. Dincer, "On-site therapeutic drug monitoring," *Trends in Biotechnology*, vol. 38, no. 11, pp. 1262–1277, 2020, ISSN: 0167-7799. DOI: 10.1016/j.tibtech.2020.03.001.
- [20] K. S. McKeating, A. Aubé, and J.-F. Masson, "Biosensors and nanobiosensors for therapeutic drug and response monitoring," *Analyst*, vol. 141, no. 2, pp. 429–449, 2015, ISSN: 0003-2654. DOI: 10.1039/c5an01861g.
- [21] M. D. Alvau, S. Tartaggia, A. Meneghello, B. Casetta, G. Calia, P. A. Serra, F. Polo, and G. Toffoli, "Enzyme-based electrochemical biosensor for therapeutic drug monitoring of anticancer drug irinotecan," *Analytical Chemistry*, vol. 90, no. 10, pp. 6012–6019, 2018, ISSN: 0003-2700. DOI: 10.1021/acs.analchem.7b04357.

- [22] F. Stradolini, T. Elboshra, A. Biscontini, G. D. Micheli, and S. Carrara, "Simultaneous monitoring of anesthetics and therapeutic compounds with a portable multichannel potentiostat," *2016 IEEE International Symposium on Circuits and Systems (ISCAS)*, pp. 834–837, 2016. DOI: 10.1109/iscas.2016.7527370.
- [23] E. Chiam, L. Weinberg, and R. Bellomo, "Paracetamol: a review with specific focus on the haemodynamic effects of intravenous administration.," *Heart, lung and vessels*, vol. 7, no. 2, pp. 121–32, 2015, ISSN: 2282-8419.
- [24] G. G. Graham and K. F. Scott, "Mechanism of action of paracetamol," *American Journal of Therapeutics*, vol. 12, no. 1, pp. 46–55, 2005, ISSN: 1075-2765. DOI: 10.1097/00045391-200501000-00008.
- [25] R. T. Stravitz and W. M. Lee, "Acute liver failure," *The Lancet*, vol. 394, no. 10201, pp. 869–881, 2019, ISSN: 0140-6736. DOI: 10.1016/s0140-6736(19)31894-x.
- [26] T. J. Athersuch, D. J. Antoine, A. R. Boobis, M. Coen, A. K. Daly, L. Possamai, J. K. Nicholson, and I. D. Wilson, "Paracetamol metabolism, hepatotoxicity, biomarkers and therapeutic interventions: a perspective," *Toxicology Research*, vol. 7, no. 3, pp. 347–357, 2018, ISSN: 2045-452X. DOI: 10.1039/c7tx00340d.
- [27] D. W. Potter and J. A. Hinson, "The 1- and 2-electron oxidation of acetaminophen catalyzed by prostaglandin h synthase.," *Journal of Biological Chemistry*, vol. 262, no. 3, pp. 974–980, 1987, ISSN: 0021-9258. DOI: 10.1016/s0021-9258(19)75736-6.
- [28] H. Shayani-Jam and D. Nematollahi, "Electrochemical evidences in oxidation of acetaminophen in the presence of glutathione and n-acetylcysteine," *Chemical Communications*, vol. 46, no. 3, pp. 409–411, 2009, ISSN: 1359-7345. DOI: 10.1039/b916458h.
- [29] D. Nematollahi, H. Shayani-Jam, M. Alimoradi, and S. Niroomand, "Electrochemical oxidation of acetaminophen in aqueous solutions: kinetic evaluation of hydrolysis, hydroxylation and dimerization processes," *Electrochimica Acta*, vol. 54, no. 28, pp. 7407–7415, 2009, ISSN: 0013-4686. DOI: 10.1016/j.electacta.2009.07.077.
- [30] J. Żur, A. Piński, A. Marchlewicz, K. Hupert-Kocurek, D. Wojcieszynska, and U. Guzik, "Organic micropollutants paracetamol and ibuprofen—toxicity, biodegradation, and genetic background of their utilization by bacteria," *Environmental Science and Pollution Research*, vol. 25, no. 22, pp. 21 498–21 524, 2018, ISSN: 0944-1344. DOI: 10.1007/s11356-018-2517-x.
- [31] T. Olcay and K. Isik, *Chemical Oxidation Applications for Industrial Wastewaters*. IWA Publishing, Oct. 2010.
- [32] B. Nunes, S. C. Antunes, J. Santos, L. Martins, and B. B. Castro, "Toxic potential of paracetamol to freshwater organisms: a headache to environmental regulators?" *Ecotoxicology and Environmental Safety*, vol. 107, pp. 178–185, 2014, ISSN: 0147-6513. DOI: 10.1016/j.ecoenv.2014.05.027.

- [33] T. Elersek, S. Milavec, M. Korošec, P. Brezovsek, N. Negreira, B. Zonja, M. L. de Alda, D. Barceló, E. Heath, J. Ščančar, and M. Filipič, "Toxicity of the mixture of selected antineoplastic drugs against aquatic primary producers," en, *Environmental Science and Pollution Research*, vol. 23, no. 15, pp. 14 780–14 790, Aug. 2016, ISSN: 1614-7499. DOI: 10.1007/s11356-015-6005-2. [Online]. Available: <https://doi.org/10.1007/s11356-015-6005-2> (visited on 08/17/2021).
- [34] K. Alanazi, A. Garcia Cruz, S. Di Masi, A. Voorhaar, O. S. Ahmad, T. Cowen, E. Piletska, N. Langford, T. J. Coats, M. R. Sims, and S. A. Piletsky, "Disposable paracetamol sensor based on electroactive molecularly imprinted polymer nanoparticles for plasma monitoring," en, *Sensors and Actuators B: Chemical*, vol. 329, p. 129 128, Feb. 2021, ISSN: 09254005. DOI: 10.1016/j.snb.2020.129128. [Online]. Available: <https://linkinghub.elsevier.com/retrieve/pii/S0925400520314672> (visited on 08/17/2021).
- [35] G. Maduraiveeran and W. Jin, "Nanomaterials based electrochemical sensor and biosensor platforms for environmental applications," *Trends in Environmental Analytical Chemistry*, vol. 13, pp. 10–23, 2017, ISSN: 2214-1588. DOI: 10.1016/j.teac.2017.02.001.
- [36] J. Claussen, J. Shi, C. S. Rout, M. Artiles, M. Roushar, M. Stensberg, D. M. Porterfield, and T. Fisher, "Biosensors for medical applications," *Part I: Principles and transduction approaches*, pp. 65–102, 2012. DOI: 10.1533/9780857097187.1.65.
- [37] E. Roduner, "Size matters: why nanomaterials are different," *Chemical Society Reviews*, vol. 35, no. 7, pp. 583–592, 2006, ISSN: 0306-0012. DOI: 10.1039/b502142c.
- [38] S. Sasidharan, S. Raj, S. Sonawane, S. Sonawane, D. Pinjari, A. Pandit, and P. Saudagar, "Nanomaterials synthesis," pp. 27–51, 2019. DOI: 10.1016/b978-0-12-815751-0.00002-x.
- [39] T. You, O. Niwa, Z. Chen, K. Hayashi, M. Tomita, and S. Hirono, "An amperometric detector formed of highly dispersed ni nanoparticles embedded in a graphite-like carbon film electrode for sugar determination," *Analytical Chemistry*, vol. 75, no. 19, pp. 5191–5196, 2003, ISSN: 0003-2700. DOI: 10.1021/ac034204k.
- [40] W. Wu, Z.-H. Huang, and T.-T. Lim, "Recent development of mixed metal oxide anodes for electrochemical oxidation of organic pollutants in water," *Applied Catalysis A: General*, vol. 480, pp. 58–78, 2014, ISSN: 0926-860X. DOI: 10.1016/j.apcata.2014.04.035.
- [41] C. Xie, D. Yan, W. Chen, Y. Zou, R. Chen, S. Zang, Y. Wang, X. Yao, and S. Wang, "Insight into the design of defect electrocatalysts: from electronic structure to adsorption energy," *Materials Today*, vol. 31, pp. 47–68, 2019, ISSN: 1369-7021. DOI: 10.1016/j.mattod.2019.05.021.
- [42] L. A. Fal'kovskii, "Physical properties of bismuth," *Soviet Physics Uspekhi*, vol. 11, no. 1, pp. 1–21, 1968, ISSN: 0038-5670. DOI: 10.1070/pu1968v011n01abeh003721.
- [43] X. Du, S.-W. Tsai, D. L. Maslov, and A. F. Hebard, "Metal-insulator-like behavior in semimetallic bismuth and graphite," *Physical Review Letters*, vol. 94, no. 16, p. 166 601, 2005, ISSN: 0031-9007. DOI: 10.1103/physrevlett.94.166601.

- [44] R. Mohan, "Green bismuth," *Nature Chemistry*, vol. 2, no. 4, pp. 336–336, 2010, ISSN: 1755-4330. DOI: 10.1038/nchem.609.
- [45] T. A. Gadhi, A. Hernández-Gordillo, M. Bizarro, P. Jagdale, A. Tagliaferro, and S. E. Rodil, "Efficient $\text{TiO}_2/\text{Bi}_2\text{O}_3$ composite for the sequential photodegradation of two-dyes mixture," *Ceramics International*, vol. 42, no. 11, pp. 13 065–13 073, 2016, ISSN: 0272-8842. DOI: 10.1016/j.ceramint.2016.05.087.
- [46] A. Walsh, G. W. Watson, D. J. Payne, R. G. Edgell, J. Guo, P.-A. Glans, T. Learmonth, and K. E. Smith, "Electronic structure of the α and β phases of Bi_2O_3 : a combined ab initio and x-ray spectroscopy study," *Physical Review B*, vol. 73, no. 23, p. 235 104, 2006, ISSN: 1098-0121. DOI: 10.1103/physrevb.73.235104.
- [47] S. S. M. Bhat and H. W. Jang, "Recent advances in bismuth-based nanomaterials for photoelectrochemical water splitting," *ChemSusChem*, vol. 10, no. 15, pp. 3001–3018, 2017, ISSN: 1864-564X. DOI: 10.1002/cssc.201700633.
- [48] M. Bartoli, P. Jagdale, and A. Tagliaferro, "A short review on biomedical applications of nanostructured bismuth oxide and related nanomaterials," *Materials*, vol. 13, no. 22, p. 5234, 2020, ISSN: 1996-1944. DOI: 10.3390/ma13225234.
- [49] T. Bruton, J. Brice, O. Hill, and P. Whiffin, "The flux growth of some Bi_2O_3 crystals by the top seeded technique," *Journal of Crystal Growth*, vol. 23, no. 1, pp. 21–24, 1974, ISSN: 0022-0248. DOI: 10.1016/0022-0248(74)90036-0.
- [50] R. Marcus and N. Sutin, "Electron transfers in chemistry and biology," en, *Biochimica et Biophysica Acta (BBA) - Reviews on Bioenergetics*, vol. 811, no. 3, pp. 265–322, Aug. 1985, ISSN: 03044173. DOI: 10.1016/0304-4173(85)90014-X. [Online]. Available: <https://linkinghub.elsevier.com/retrieve/pii/030441738590014X> (visited on 04/09/2021).
- [51] J. J. Hopfield, "Electron Transfer Between Biological Molecules by Thermally Activated Tunneling," en, *Proceedings of the National Academy of Sciences*, vol. 71, no. 9, pp. 3640–3644, Sep. 1974, ISSN: 0027-8424, 1091-6490. DOI: 10.1073/pnas.71.9.3640. [Online]. Available: <http://www.pnas.org/cgi/doi/10.1073/pnas.71.9.3640> (visited on 04/08/2021).
- [52] R. Holze, "Elektronentransfer: *Surface Electron Transfer Processes*. Von R. J. D. Miller, G. L. McLendon, A. Nozik, W. Schmickler und F. Willig. VCH, Weinheim, 1995. 370 S., geb., 128,-DM. ISBN 1-56081-036-X," en, *Nachrichten aus Chemie, Technik und Laboratorium*, vol. 44, no. 6, pp. 634–635, Jun. 1996, ISSN: 03415163. DOI: 10.1002/nadc.19960440624. [Online]. Available: <http://doi.wiley.com/10.1002/nadc.19960440624> (visited on 04/08/2021).
- [53] E. G. Lewars, *Computational Chemistry: Introduction to the Theory and Applications of Molecular and Quantum Mechanics*, 3rd ed. 2016. Cham: Springer International Publishing : Imprint: Springer, 2016, ISBN: 9783319309163.
- [54] J. W. Evenson and M. Karplus, "Effective coupling in bridged electron transfer molecules: Computational formulation and examples," en, *The Journal of Chemical Physics*, vol. 96, no. 7, pp. 5272–5278, Apr. 1992, ISSN: 0021-9606, 1089-7690. DOI: 10.1063/1.462712. [Online]. Available: <http://aip.scitation.org/doi/10.1063/1.462712> (visited on 06/29/2021).

- [55] J. Evenson and M. Karplus, "Effective coupling in biological electron transfer: exponential or complex distance dependence?" en, *Science*, vol. 262, no. 5137, pp. 1247–1249, Nov. 1993, ISSN: 0036-8075, 1095-9203. DOI: 10.1126/science.8235654. [Online]. Available: <https://www.sciencemag.org/lookup/doi/10.1126/science.8235654> (visited on 06/29/2021).
- [56] Y. Georgievskii, C.-P. Hsu, and R. A. Marcus, "Linear response in theory of electron transfer reactions as an alternative to the molecular harmonic oscillator model," en, *The Journal of Chemical Physics*, vol. 110, no. 11, pp. 5307–5317, Mar. 1999, ISSN: 0021-9606, 1089-7690. DOI: 10.1063/1.478425. [Online]. Available: <http://aip.scitation.org/doi/10.1063/1.478425> (visited on 04/09/2021).
- [57] R. A. Marcus, "Chemical and Electrochemical Electron-Transfer Theory," en, *Annual Review of Physical Chemistry*, vol. 15, no. 1, pp. 155–196, Oct. 1964, ISSN: 0066-426X, 1545-1593. DOI: 10.1146/annurev.pc.15.100164.001103. [Online]. Available: <http://www.annualreviews.org/doi/10.1146/annurev.pc.15.100164.001103> (visited on 04/08/2021).
- [58] Y. Dakhnovskii, "Dynamics of inner- and outer-sphere electron transfer in a polar solvent," en, *Journal of Molecular Liquids*, vol. 60, no. 1-3, pp. 73–86, Jul. 1994, ISSN: 01677322. DOI: 10.1016/0167-7322(94)00740-3. [Online]. Available: <https://linkinghub.elsevier.com/retrieve/pii/0167732294007403> (visited on 04/09/2021).
- [59] W. F. Libby, "Theory of Electron Exchange Reactions in Aqueous Solution," en, *The Journal of Physical Chemistry*, vol. 56, no. 7, pp. 863–868, Jul. 1952, ISSN: 0022-3654, 1541-5740. DOI: 10.1021/j150499a010. [Online]. Available: <https://pubs.acs.org/doi/abs/10.1021/j150499a010> (visited on 04/09/2021).
- [60] R. A. Marcus, "On the Theory of Oxidation-Reduction Reactions Involving Electron Transfer. I," en, *The Journal of Chemical Physics*, vol. 24, no. 5, pp. 966–978, May 1956, ISSN: 0021-9606, 1089-7690. DOI: 10.1063/1.1742723. [Online]. Available: <http://aip.scitation.org/doi/10.1063/1.1742723> (visited on 04/18/2021).
- [61] R. A. Marcus, "Electron Transfer Reactions in Chemistry: Theory and Experiment (Nobel Lecture)," en, *Angewandte Chemie International Edition in English*, vol. 32, no. 8, pp. 1111–1121, 1993, ISSN: 1521-3773. DOI: <https://doi.org/10.1002/anie.199311113>. [Online]. Available: <https://onlinelibrary.wiley.com/doi/abs/10.1002/anie.199311113> (visited on 04/08/2021).
- [62] M. Tachiya, "Generalization of the Marcus equation for the electron-transfer rate," en, *The Journal of Physical Chemistry*, vol. 97, no. 22, pp. 5911–5916, Jun. 1993, ISSN: 0022-3654, 1541-5740. DOI: 10.1021/j100124a023. [Online]. Available: <https://pubs.acs.org/doi/abs/10.1021/j100124a023> (visited on 06/28/2021).
- [63] M. Tachiya and M. Hilczer, "Solvent effect on the electron transfer rate and the energy gap law," en, in *AIP Conference Proceedings*, vol. 298, Royanmont (France): AIP, 1994, pp. 447–459. DOI: 10.1063/1.45399. [Online]. Available: <http://aip.scitation.org/doi/abs/10.1063/1.45399> (visited on 06/28/2021).

- [64] J. Ulstrup, *Charge Transfer Processes in Condensed Media*, G. Berthier, M. J. S. Dewar, H. Fischer, K. Fukui, H. Hartmann, H. H. Jaffé, J. Jortner, W. Kutzelnigg, K. Ruedenberg, E. Scrocco, and W. Zeil, Eds., ser. Lecture Notes in Chemistry. Berlin, Heidelberg: Springer Berlin Heidelberg, 1979, vol. 10, ISBN: 9783540095200 9783642931161. DOI: 10.1007/978-3-642-93116-1. [Online]. Available: <http://link.springer.com/10.1007/978-3-642-93116-1> (visited on 06/28/2021).
- [65] R. J. Cave and M. D. Newton, "Generalization of the Mulliken-Hush treatment for the calculation of electron transfer matrix elements," en, *Chemical Physics Letters*, vol. 249, no. 1-2, pp. 15–19, Jan. 1996, ISSN: 00092614. DOI: 10.1016/0009-2614(95)01310-5. [Online]. Available: <https://linkinghub.elsevier.com/retrieve/pii/0009261495013105> (visited on 06/28/2021).
- [66] R. Hoffmann, "An extended hückel theory. i. hydrocarbons," *The Journal of Chemical Physics*, vol. 39, no. 6, pp. 1397–1412, 1963, ISSN: 0021-9606. DOI: 10.1063/1.1734456.
- [67] A. J. Bard and L. R. Faulkner, *Electrochemical Methods: Fundamentals and Applications*, ISBN: 9780471043720.
- [68] T. Tangkuaram, C. Ponchio, T. Kangkasomboon, P. Katikawong, and W. Veerasai, "Design and development of a highly stable hydrogen peroxide biosensor on screen printed carbon electrode based on horseradish peroxidase bound with gold nanoparticles in the matrix of chitosan," *Biosensors and Bioelectronics*, vol. 22, no. 9-10, pp. 2071–2078, 2007, ISSN: 0956-5663. DOI: 10.1016/j.bios.2006.09.011.
- [69] H. Kodama, "Synthesis of a New Compound, Bi₅O₇NO₃, by Thermal Decomposition," *Journal of Solid State Chemistry*, vol. 112, no. 1, pp. 27–30, 1994, ISSN: 0022-4596. DOI: 10.1006/jssc.1994.1259.
- [70] P. T. Kissinger and W. R. Heineman, "Cyclic voltammetry," *Journal of Chemical Education*, vol. 60, no. 9, p. 702, 1983, ISSN: 0021-9584. DOI: 10.1021/ed060p702.
- [71] D. H. Evans, K. M. O'Connell, R. A. Petersen, and M. J. Kelly, "Cyclic voltammetry," *Journal of Chemical Education*, vol. 60, no. 4, p. 290, 1983, ISSN: 0021-9584. DOI: 10.1021/ed060p290.
- [72] M. B. Gholivand and A. Azadbakht, "A novel hydrazine electrochemical sensor based on a zirconium hexacyanoferrate film-bimetallic au-pt inorganic-organic hybrid nanocomposite onto glassy carbon-modified electrode," *Electrochimica Acta*, vol. 56, no. 27, pp. 10 044–10 054, 2011, ISSN: 0013-4686. DOI: 10.1016/j.electacta.2011.08.098.
- [73] H. Kahlert, U. Retter, H. Lohse, K. Siegler, and F. Scholz, "On the determination of the diffusion coefficients of electrons and of potassium ions in copper(ii) hexacyanoferrate(ii) composite electrodes," *The Journal of Physical Chemistry B*, vol. 102, no. 44, pp. 8757–8765, 1998, ISSN: 1520-6106. DOI: 10.1021/jp981623q.
- [74] H. Heli, S. Majdi, and N. Sattarahmady, "Ultrasensitive sensing of n-acetyl-l-cysteine using an electrocatalytic transducer of nanoparticles of iron(iii) oxide core-cobalt hexacyanoferrate shell," *Sensors and Actuators B: Chemical*, vol. 145, no. 1, pp. 185–193, 2010, ISSN: 0925-4005. DOI: 10.1016/j.snb.2009.11.065.

- [75] O. A. González-Meza, E. R. Larios-Durán, A. Gutiérrez-Becerra, N. Casillas, J. I. Escalante, and M. Bárcena-Soto, "Development of aandles-ševčík-like equation to predict the peak current of cyclic voltammetry for solid metal hexacyanoferrates," *Journal of Solid State Electrochemistry*, vol. 23, no. 11, pp. 3123–3133, 2019, ISSN: 1432-8488. DOI: 10.1007/s10008-019-04410-6.
- [76] E. Laviron, "General expression of the linear potential sweep voltammogram in the case of diffusionless electrochemical systems," *Journal of Electroanalytical Chemistry and Interfacial Electrochemistry*, vol. 101, no. 1, pp. 19–28, 1979, ISSN: 0022-0728. DOI: 10.1016/s0022-0728(79)80075-3.
- [77] P. Ziegler, M. Ströbele, and H.-J. Meyer, "Crystal structure of pentabismuth heptaoxide nitrate, Bi₅O₇NO₃," *Zeitschrift für Kristallographie - New Crystal Structures*, vol. 219, no. 1-4, pp. 101–102, Apr. 2004, ISSN: 2197-4578, 1433-7266. DOI: 10.1524/ncrs.2004.219.14.101. [Online]. Available: <https://www.degruyter.com/document/doi/10.1524/ncrs.2004.219.14.101/html> (visited on 04/29/2021).
- [78] T. A. Gadhi, S. Hernández, M. Castellino, P. Jagdale, T. Husak, A. Hernández-Gordillo, A. Tagliaferro, and N. Russo, "Insights on the role of -Bi₂O₃/Bi₅O₇NO₃ heterostructures synthesized by a scalable solid-state method for the sunlight-driven photocatalytic degradation of dyes," en, *Catalysis Today*, vol. 321-322, pp. 135–145, Feb. 2019, ISSN: 09205861. DOI: 10.1016/j.cattod.2017.12.038. [Online]. Available: <https://linkinghub.elsevier.com/retrieve/pii/S0920586117308659> (visited on 04/29/2021).
- [79] X. Liu and K. Sohlberg, "Empirical correction for PM7 band gaps of transition-metal oxides," en, *Journal of Molecular Modeling*, vol. 22, no. 1, p. 24, Jan. 2016, ISSN: 1610-2940, 0948-5023. DOI: 10.1007/s00894-015-2891-y. [Online]. Available: <http://link.springer.com/10.1007/s00894-015-2891-y> (visited on 04/29/2021).
- [80] H. Kodama, "Synthesis of a New Compound, Bi₅O₇NO₃, by Thermal Decomposition," *Journal of Solid State Chemistry*, vol. 112, no. 1, pp. 27–30, 1994, ISSN: 0022-4596. DOI: 10.1006/jssc.1994.1259.
- [81] A. K. S. Kumar, Y. Zhang, D. Li, and R. G. Compton, "A mini-review: how reliable is the drop casting technique?" *Electrochemistry Communications*, vol. 121, p. 106867, 2020, ISSN: 1388-2481. DOI: 10.1016/j.elecom.2020.106867.
- [82] M. Madagalam, M. Bartoli, A. Tagliaferro, and S. Carrara, "Bismuth-nanocomposites modified spces for non-enzymatic electrochemical sensors," *IEEE Sensors Journal*, vol. 21, no. 9, pp. 11155–11162, 2021, ISSN: 1530-437X. DOI: 10.1109/jsen.2021.3059278.
- [83] M. D. Fontana, K. B. Mabrouk, and T. Kauffmann, "Raman probe of pollutants in water: measurement process," in *IMEKO TC19*, Jun. 2013.
- [84] K. Nakamoto, "Infrared and raman spectra of inorganic and coordination compounds," 2018. DOI: 10.1002/9780470405840.
- [85] S. Rossignol, C. Descorme, C. Kappenstein, and D. Duprez, "Synthesis, structure and catalytic properties of zr–ce–pr–o mixed oxides," *Journal of Materials Chemistry*, vol. 11, no. 10, pp. 2587–2592, 2001, ISSN: 0959-9428. DOI: 10.1039/b102763h.

- [86] A. P. Kotula, C. R. Snyder, and K. B. Migler, "Determining conformational order and crystallinity in polycaprolactone via raman spectroscopy," *Polymer*, vol. 117, pp. 1–10, 2017, Utile per la comprensione dello shift dei picchi raman, ISSN: 0032-3861. DOI: 10.1016/j.polymer.2017.04.006.